Coatings **2013**, *3*, 268-300; doi:10.3390/coatings3040268

OPEN ACCESS

coatings

ISSN 2079-6412

www.mdpi.com/journal/coatings

Article

Gas Permeation, Mechanical Behavior and Cytocompatibility of Ultrathin Pure and Doped Diamond-Like Carbon and Silicon Oxide Films

Juergen M. Lackner [1], Claudia Meindl [3], Christian Wolf [2], Alexander Fian [2], Clemens Kittinger [4], Marcin Kot [6], Lukasz Major [7], Caterina Czibula [8], Christian Teichert [8], Wolfgang Waldhauser [1], Annelie-Martina Weinberg [5], Eleonore Fröhlich [3,*]

1 Group of Functional Surfaces, Institute of Surface Technologies and Photonics, JOANNEUM RESEARCH Forschungsges.m.b.H., Leobner Strasse 94, A-8712 Niklasdorf, Austria; E-Mails: juergen.lackner@joanneum.at (J.M.L.); wolfgang.waldhauser@joanneum.at (W.W.)

2 Institute of Surface Technologies and Photonics, JOANNEUM RESEARCH Forschungsges.m.b.H., Franz-Pichler-Strasse 30, A-8160 Weiz, Austria; E-Mails: christian.wolf@joanneum.at (C.W.); alexander.fian@joanneum.at (A.F.)

3 Center for Medical Research, Medical University Graz, Stiftingtalstrasse 24, A-8010 Graz, Austria; E-Mail: claudia.meindl@klinikum-graz.at

4 Institute of Hygiene, Microbiology and Environmental Medicine, Medical University Graz, Universitätsplatz 4, A-8010 Graz, Austria; E-Mail: Clemens.kittinger@medunigraz.at

5 Department of Orthopedics and Orthopedic Surgery, Medical University Graz, Auenbruggerplatz 5, A-8010 Graz, Austria; E-Mail: Annelie.Weinberg@t-online.de

6 Faculty of Mechanical Engineering and Robotics, AGH University of Science and Technology, 30 Adama Mickiewicza Av., 30-059 Cracow, Poland; E-Mail: kotmarc@imir.agh.edu.pl

7 Institute of Metallurgy and Materials Sciences, Polish Academy of Sciences, ul. Reymonta 25, 30-059 Krakow, Poland; E-Mail: nmlmajor@imim-pan.krakow.pl

8 Institute of Physics, University of Leoben, Franz Josef Strasse 18, A-8700 Leoben, Austria; E-Mails: caterina-marina.czibula@stud.unileoben.ac.at (C.C.); Teichert@unileoben.ac.at (C.T.)

***** Author to whom correspondence should be addressed; E-Mail: eleonore.froehlich@medunigraz.at.

Received: 17 September 2013; in revised form: 20 November 2013 / Accepted: 6 December 2013 / Published: 16 December 2013

Abstract: Protective ultra-thin barrier films gather increasing economic interest for controlling permeation and diffusion from the biological surrounding in implanted sensor and electronic devices in future medicine. Thus, the aim of this work was a benchmarking

of the mechanical oxygen permeation barrier, cytocompatibility, and microbiological properties of inorganic ~25 nm thin films, deposited by vacuum deposition techniques on 50 µm thin polyetheretherketone (PEEK) foils. Plasma-activated chemical vapor deposition (direct deposition from an ion source) was applied to deposit pure and nitrogen doped diamond-like carbon films, while physical vapor deposition (magnetron sputtering in pulsed DC mode) was used for the formation of silicon as well as titanium doped diamond-like carbon films. Silicon oxide films were deposited by radio frequency magnetron sputtering. The results indicate a strong influence of nanoporosity on the oxygen transmission rate for all coating types, while the low content of microporosity (particulates, *etc.*) is shown to be of lesser importance. Due to the low thickness of the foil substrates, being easily bent, the toughness as a measure of tendency to film fracture together with the elasticity index of the thin films influence the oxygen barrier. All investigated coatings are non-pyrogenic, cause no cytotoxic effects and do not influence bacterial growth.

Keywords: thin films; diamond-like carbon; permeability; cytocompatibility

1. Introduction

Finding materials with both high biocompatibility (cytocompatibility, hemocompatibility, *etc.*) and low or controllable gas permeation is a great challenge for using microelectronics and microfluidics in *in vivo* sensors. Microelectronic devices are generally based on a large number of materials for electronics and printed circuit boards, including ceramics and polymers for chip and resistor housings, metal and semiconductors for the chip itself, metals (Al, Ni-Au, Pd-Au, Cu, Pd-Cu, *etc.*) for circuit paths, fiber reinforced epoxy binders, polyimide and polyurethane foils for dielectrics and various glues. Only a few of them are biocompatible, as shown in tests with hippocampus cells by Mazzuferi *et al.* [1]. Thus, dense packaging for any *in vivo* use is essential to prevent permeation/diffusion of body fluids into the electronic components. This saves the electronics from biological fluids as well as the tissue from any (corrosion) contaminants from the electronics.

Packaging by metal or polymer housings is state-of-the-art, but limited in miniaturization. Coatings are alternatives to such robust housings, but they must prove their applicability both for biocompatibility and for long-term permeation and corrosion protection. In recent years, polymers like polydimethylsiloxane, parylene-C and polymethyl methacrylate have been applied on silicon based devices due to easy manufacturing, sufficiently high mechanical properties and bio-inertness. However, their barrier properties are limited, as shown for parylene-C in contact with blood [2]. Polyelectrolyte layers are generally robust, but possess no long-term stability [3,4]. Plasmapolymer layers, deposited from hydrocarbon, silicon and titanium containing organic compounds or monomers like tetraglyme, are generally free of pin-holes and possess good barrier properties. Their adhesion to microelectronic substrate materials is high [5]. Inorganic thin films based on SiO_2 and SiN are frequently used as permeation protective coatings for microelectronic and microfluidic devices due to their bio-inert behavior, missing cytotoxicity and high barrier effect [6–11]. Other well-known vacuum

coating materials, deposited by physical and chemical vapor deposition (PVD, CVD) are platinum, gold, titanium oxide and other ceramics like aluminum oxide and oxynitride [12–14]. Further improvements in gas barrier are provided by multilayered film structures based on inorganic and organic layers [15–17]. Ultra-thin and dense films can be grown by atomic layer deposition (e.g. Al_2O_3, SiC, TiO_2 [18]). However, they have application limitations for low-temperature resistant substrates like polymers due to the required high temperatures for precursor dissociation. Similar problem exists for ultra nanocrystalline diamond thin films, which have a high gas permeation barrier and are not cytotoxic, but require 400–800 °C temperature for phase formation during deposition. In contrast, diamond-like carbon based materials (DLC) require only lower temperatures for film growth. Such DLC coatings are generally amorphous and are characterized by a mixture of sp^2 and sp^3 hybridized carbon atoms and, mostly, hydrogen (a-C:H). However, physical and chemical influences on their biocompatibility have not yet been fully solved, as described in a review on about 90 different DLC materials [19]. Nevertheless, the cytotoxicity of DLC materials is very low with no *in vitro* effects on mouse macrophages, human fibroblasts, monocytes, osteoblasts [20,21] even under *in vivo* conditions in subcutaneous, bone and muscle tissue in guinea pig [22], sheep and rat models [23]). Doping DLC films with fluorine is favorable and results in antithrombotic effects and the suppression of platelet activation [24]. N or Si doping improves the endothelium cell growth and provides antithrombotic effects [25–29].

The goal of this work is a comparative study of different a-C:H materials (pure and N, Si, and Ti doped a-C:H), deposited as very thin films on polymers by high vacuum coating techniques (direct deposition from ion sources and magnetron sputtering) to correlate effects of the film material, structure and toughness on the gas permeation barrier properties as well as chemical composition and surface topography on the biocompatibility.

2. Materials and Methods

2.1. Substrate Materials

Polyether etherketone (PEEK) polymer thin foils (Victrex Aptiv 1000) with 50 µm thickness, silicon (100) wafer with 525 µm thickness, and biocompatible glass (Schott Borofloat 33: 81% SiO_2, 13% B_2O_3, 4% Na_2O/K_2O, and 2% Al_2O_3) were chosen as substrate materials for the investigations. The PEEK foils are semi-crystalline, non-filled, medical-grade polymers with an elastic modulus of 2500 MPa and a tensile strength of 120 MPa at >150% strain (tensile tests according to ISO 527 [30]). They are well suitable for future microelectronic applications due to a high dielectric strength of 190 kV mm^{-1} (ASTM D149 test) and a dielectric constant of 3.4 (ASTM D150 test). The water absorption (ASTM D696 test) is around 0.04%, which excludes significant changes in mechanical properties in the humid and wet environment. The permeability of oxygen (oxygen transmission rate, OTR) is >200 $cm^3\ m^{-2}\ d^{-1}$ for 50 µm thick foils.

2.2. Film Deposition

The deposition of 26 ± 3 nm thick coatings was carried out by high vacuum coating techniques in a semi-industrial coating machine. This equipment is equipped with magnetron sputtering (PVD process

by sputtering of a solid target) and direct deposition from ion source plasma (plasma activated CVD process based on dissociation of a hydrocarbon precursor). A schematic view of the arrangement of the deposition sources in the coating machine is shown in Figure 1. Continuous rotation during the coating operation guarantees highest homogeneity in thickness and chemical composition (>97%) over the whole coated surface [31].

Figure 1. Schematic top view of the vacuum coating machine, showing the position of sputtering cathodes, anode layer ion source (ALS) and substrate table (planetary).

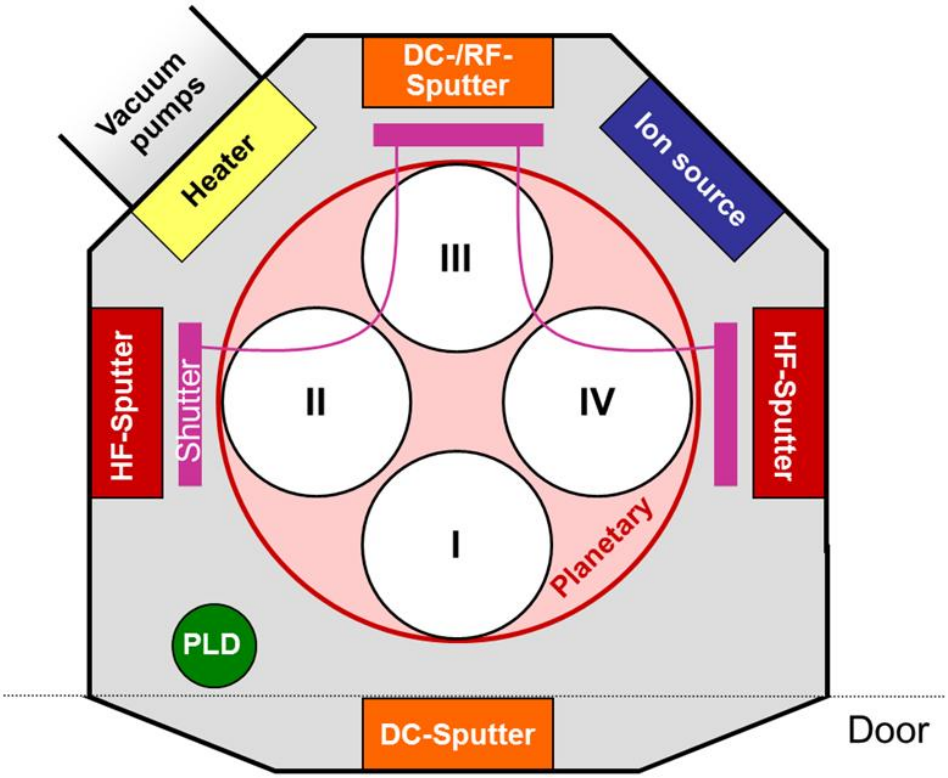

Before coating, the substrates were cleaned with ethanol and dried in nitrogen. After mounting on the substrate table (fixing on four edges with adhesive tape) at 100 mm distance to the coating sources (magnetron sputtering target and ion source, respectively), the evacuation to 2×10^{-3} Pa base pressure was begun. A plasma activation of the substrate surfaces occurred subsequently by an anode layer ion source (ALS) in oxygen plasma to guarantee high film adhesion. The following step for film deposition was chosen individually depending on the specific film material:

1) a-C:H: direct deposition from the ALS ion source plasma at 1 kV in ethine (1×10^{-1} Pa, 0.44 nm min^{-1} deposition rate);
2) a-C:H:N: direct deposition from the ALS ion source plasma at 1 kV in a gas mixture of 75% ethine and 25% nitrogen (1×10^{-1} Pa, 0.25 nm min^{-1} deposition rate);
3) a-C:H:Si: magnetron sputtering in pulsed DC (direct current) mode (80 kHz, 1.4 kW) from a silicon target in a gas mixture of 40% ethine and 60% argon (4×10^{-1} Pa, 6.8 nm min^{-1} deposition rate);

4) a-C:H:Ti: magnetron sputtering in pulsed DC mode (80 kHz, 1.4 kW) from a titanium target (grade-2 titanium) in a gas mixture of 40% ethine and 60% argon (4×10^{-1} Pa, 11.4 nm min^{-1} deposition rate);
5) SiO_x: magnetron sputtering in RF (radio frequency) mode (13.56 MHz, 300 W) from a silicon target in a mixture of 15% oxygen and 85% argon (4×10^{-1} Pa, 6.3 nm min^{-1} deposition rate).

During pretreatment and coating, the substrates were grounded without the application of substrate biasing.

After coating, all samples for biocompatibility and microbiological testing were sterilized by gamma radiation.

2.3. Film Characterization

2.3.1. Characterization of Chemical Film Composition

The determination of the chemical film composition was carried out by X-ray photo-electron spectroscopy (XPS) with an Omicron Multiprobe system. Films on silicon substrates were irradiated in high vacuum (4×10^{-9} Pa) by a monochromatic AlKα X-ray beam (1486.6 eV). Energetic measurements of the emitted photoelectrons occurred with an EA 125 analyzer in "fixed analyzer mode" with a spectral resolution better than 0.3 eV and a detection sensitivity of about 1 wt%. Fitting of the energy spectra provided the elemental concentration of C, O, Si, Ti, and N. Because H is not measurable by XPS, the sum of the given elemental concentration of these elements was set to 100%.

The chemical binding analysis of the carbon thin films was carried out by Raman spectroscopy on a Horiba Jobin Yvon LabRam Raman Microspectrometer system for films on silicon substrates. After excitation with a 532 nm Nd:YAG laser (1 μm laser spot diameter on the surface, 0.01 mW power), the analysis of the scattered light occurred by a 1024 × 256 CCD open electrode detector with a spectral resolution of about 5 cm^{-1} (1000 μm confocal aperture, entrance slit 100 μm). The calibration was carried out by a Ne spectral lamp, leading to 0.5 cm^{-1} accuracy of the Raman shifts. The peak fitting with Gauss-Lorentz functions and the linear background correction was carried out with the Labspec 5 software package.

2.3.2. Structural and Topographical Film Characterization

The film structure was investigated by high-resolution transmission electron microscopy [HR-TEM, Tecnai G2 F20 (200 kV FEG), FEI Co., Hillsboro, OR, USA], using small angle electron diffraction (SAED) for structural investigations.

All film thickness measurements were performed on a stylus profiler (Dektak 150, Veeco Metrology, Santa Barbara, CA, USA) at masked steps. Light microscopy enlightened defects (e.g., pin-holes, defects) on coated PEEK substrates after cleaning in nitrogen to remove dust. Detailed scans of the surface topography and the determination of quantitative topographical data on the nano- and micro scale were performed by atomic force microscopy (AFM, MFP 3D, Asylum Research, Goleta, CA, USA) in tapping mode with Olympus AC 240 TS silicon tips (tip radius <15 nm). The analysis of the acquired data was carried out using the software package Gwyddion [32] in order to obtain both the amplitude parameters (geometrical/root mean square roughness, RMS, σ) to describe the height

differences and the lateral frequency parameters (lateral correlation length, ξ [33]). While vertical roughness parameters and their calculation are generally known, lateral frequency parameters have been scarcely used as yet to describe the surface topography, although a lot of physicochemical phenomena on the surface, e.g., peak densities, are strongly influenced by distances between the peaks and short-range order. For a random rough surface with a cut-off, the lateral frequency of roughness is described by the lateral correlation length, which is a measure of the lateral distance across which the height of the surfaces are correlated [34]. Generally, it corresponds to the minimum lateral feature size and is smaller than the average feature size [35].

2.3.3. Characterization of Mechanical Film Properties

The mechanical properties were determined by instrumented micro-indentation testing with 1 mN maximum force on a Vickers diamond, applying CSM Instruments MCT equipment. Oliver-Pharr theories [36] were chosen to calculate both the elastic modulus and the hardness values from indentation results in the thin films and the fused silica calibration standard. To minimize substrate influences, films with 800–1000 nm thickness were deposited on a silicon substrate and used for measurements, for which 150 nm depth was set as maximum indentation depth to exclude substrate influences. For statistics, six indentations were carried out on each sample. The film toughness on silicon was measured based on the indentation method by a Berkovich diamond, described by Li *et al.* [37,38]. The threshold force for the onset of cohesive film fracture, which can be correlated to steps in the load-indentation curve, was defined as a measure of the fracture toughness of the films.

The determination of the wetting behavior was carried out with four liquids of different surface tension (distilled water, ethylene glycol, benzyl alcohol, glycerin) at 25 °C temperature and 55% relative humidity about seven days after film deposition to include surface oxidation, relaxation and aging effects in the results. Storage in ambient air atmosphere during this duration occurred under controlled conditions of 20 °C and 50% relative humidity. The statistics of these investigations is based on a minimum of three independent measurements on different surface areas. For measuring the water contact angles with smaller droplet sizes, a Krüss DSA 100M Picoliter system was used under the same measurement conditions (droplet size: 100 pL, HPLC water).

2.3.4. Characterization of Gas Permeation through Films

Gas permeation rates of oxygen through the coated, 50 µm thick PEEK foils were measured optochemically: The applied sensor is based on an oxygen-sensitive luminescence color (palladium(II)-5,10,15,20-tetrakis-(2,3,4,5,6-pentafluorphenyl)-porphyrin) in high permeable matrix [39,40], whereby the luminescence depends on the oxygen concentration. The samples (the uncoated reference as well as coated PEEK foils) are situated in between two chambers, of which one is filled with pure oxygen (>99.999%) and the other with pure nitrogen (>99.999%). This second chamber contains the luminescence color sensor and it is cleaned from any oxygen contamination before the measurement by long nitrogen purging. The permeation through the sample increases the oxygen concentration in this chamber. Pulsed light from two green LEDs, introduced through a glass window, is used to trigger the luminescence in the sensor and to supply a reference signal for the photo

detector (Figure 2). Both intensity and duration of the luminescence are dependent on the oxygen concentration, being the basis for the calculation of the OTR value.

Figure 2. Setup of the optochemical permeation test probe [39].

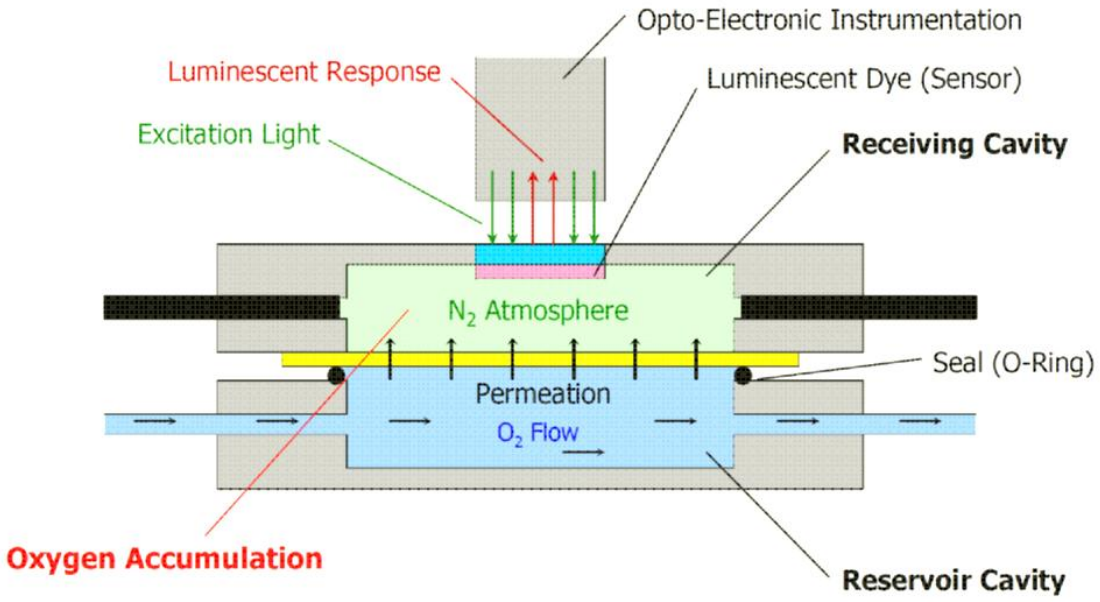

2.3.5. Biocompatibility Characterization

2.3.5.1. Detection of Endotoxin

Detection of endotoxin was performed in compliance to ISO 10993-1, -12 [41,42]. Three cm^2 of foil surface was extracted per mL pyrogen-free water for 24 ± 1 h at 37 ± 1 °C. PYROGENT Ultra (sensitivity = 0.06 EU/mL, Lonza) was used for the endotoxin testing. This clotting test can be used for all kinds of samples. It is a qualitative test for Gram-negative bacterial endotoxin, which can produce quantitative data, if serial dilutions of the samples are tested. The mechanism is the following: Gram-negative bacterial endotoxin catalyzes the activation of a proenzyme in the Limulus Amebocyte Lysate. The initial rate of activation is determined by the concentration of endotoxin. The activated enzyme (coagulase) hydrolyzes specific bonds within a clotting protein (coagulogen) also present in Limulus Amebocyte Lysate. Once hydrolyzed, the resultant coagulin self-associates and forms a gelatinous clot.

Each sample dilution was tested in duplicate, and the different endotoxin standards with E.coli strain 055:B5 in triplicates. The assay is performed first as a yes/no test and samples with positive endotoxin detection are further tested via a dilution series to quantify free endotoxin. An amount of 100 µL of standard, water, and samples together with 100 µL of the reconstitute lysate were added to each tube and placed at 37 ± 1 °C in a non-circulating water bath. After one hour (±2 min) of incubation, each tube was examined for gelation. A positive reaction is characterized by the formation of a firm gel (Figure 3, lower tube), which remains intact if the tube is inverted (vertical rotation of 180 °). A negative reaction is characterized by the absence of a solid clot after inversion (Figure 3, upper tube). The reaction of each tube is recorded as either positive or negative.

Figure 3. (**a**) Lack of coagulation in the absence of endotoxin and (**b**) formation of a firm clot at a concentration of 0.125 EU/mL.

2.3.5.2. Cytotoxicity Testing

1) Cell Lines

Tests were carried out using human MRC-5 (ATCC® CCL-171™) and murine L929 (ATCC® CCL-1™) fibroblasts. MRC-5 cells were cultured in 175 cm^2 culture flasks (Costar Corning) in Minimal Essential Medium (MEM, PAA) + Earle's salts, 10% fetal bovine serum (PAA), 2mM L-glutamine, 2% penicillin/streptomycin at 37 ± 1 ℃ and 5% CO_2. For L929 cells, DMEM (PAA) + 10% fetal bovine serum (PAA), 2mM L-glutamine, 2% penicillin/streptomycin was used. The MRC-5 cell line was derived from normal lung tissue of a 14-week-old male fetus [43]. The L929 cell line was generated from normal subcutaneous areolar and adipose tissue of a 100 day old male C3H/An mouse [44].

2) Cytotoxicity Screening of Eluates/Extracts

The detection with the CellTiter 96® AQueous Non-Radioactive Cell Proliferation Assay uses a novel tetrazolium compound (3-(4,5-dimethylthiazol-2-yl)-5-(3-carboxymethoxyphenyl)-2-(4-sulfophenyl)-2H-tetrazolium, inner salt; MTS) and an electron coupling reagent (phenazine methosulfate; PMS). MTS is bioreduced by cellular dehydrogenases into a formazan product, which is soluble in the tissue culture medium and can be quantified by photometric measurement.

Eluates from the test materials were obtained by incubation of 3 cm^2 foil surface per ml MEM Earle's salts, 10% fetal bovine serum (PAA), 2mM L-glutamine (MRC-5 cells) or DMEM, 10% fetal bovine serum, 2 mM L-glutamine (L929 cells) for 24 ± 1 h at 37 ± 1 ℃. The extraction was carried out in compliance with ISO 10993-5 and ISO 10993-12 regulations [42,45]. Subconfluent cultures must be tested for optimal assessment of cytotoxicity. To avoid overgrowth of the cells with subsequent growth inhibition at later evaluation time points, different numbers of cells were seeded: MRC-5 Cells were seeded at densities of 16,000/well for 24 h exposure, 13,000/well for 48 h exposure, and 11,000/well for 72 h exposure in 96-well plates and pre-cultured for 24 h. L929 cells were seeded at densities of 18,000/well for 24 h exposure, 12,000/well for 48 h exposure, and 6000/well for 72 h exposure in 96-well plates and pre-cultured for 24 h too. Pure eluates and diluted eluates with concentrations of 1:2, 1:5, and 1:10 were added to the cells and cultured for 24 h, 48 h,

and 72 h afterwards. Samples of 20 nm plain polystyrene particles (Thermo Scientific) were used as positive control and 200 nm plain polystyrene particles (Thermo Scientific) as negative control. CellTiter 96® AQueous Non-Radioactive Cell Proliferation Assay (Promega) was used for the testing. The MTS solution and the PMS solution were thawed, 100 µL of the PMS solution was mixed with 2 mL of MTS solution and 20 µL of the combined MTS/PMS solution was added to 100 µL of each well. Plates were incubated for 2 h at 37 ± 1 °C and 5% CO_2 in a cell incubator. Absorbance was read at 490 nm on a plate reader (SPECTRA MAX plus 384, Molecular Devices). In parallel, cells were viewed by brightfield microscopy to confirm the MTS data. Dehydrogenase activity as indication for cell viability was calculated according to the following formula (Equation 1):

$$\text{Dehydrogenase Activity (\%)} = 100 \times \frac{(A_{490\text{ nm}}\ \text{sample}) - (A_{490\text{ nm}}\ \text{blank})}{(A_{490\text{ nm}}\ \text{control}) - (A_{490\text{ nm}}\ \text{blank})} \quad (1)$$

Indication for cytotoxic effect according to ISO 10993-5 [45] is a dehydrogenase activity of less than 70% compared to untreated controls (solvent controls).

3) Cytotoxicity Screening in Direct Contact

MRC-5 Cells were seeded at densities of 200,000/well and L929 cells were seeded at densities of 240,000/well in 6-well plates 24 h prior to the experiment to reach confluence. For the evaluation in direct contact, 1.3 ± 0.2 cm^2 of test material/well, covering ~1/7th of the growth area as suggested in other studies was applied [46]. A copper foil (Glas-per-Klick) served as positive control and a PVC foil (cell culture plastic ware, PAA) as negative control. The controls and test samples (coated PEEK) were placed on the cell layer for 24 h at 37 ± 1 °C and 5% CO_2. After the removal of the controls and the samples, cells were viewed in phase contrast to evaluate the cell density and the morphology. Subsequently, the cells were stained with 0.2% crystal violet (Merck) for 20 min at RT and washed. The coverage of the plate with cells and the cellular morphology were recorded.

Any defects of ≥1 cm beyond the test material in combination with morphological alterations of the cells were interpreted as cytotoxic effects. The morphological evaluation of the cells was performed according to the grading system used for Biological Reactivity Tests *in vitro* (Table 1) [47]. This test system is suitable, if the observed responses to the negative control are grade 0 (no reactivity) and the responses to the positive control are at least grade 3 (moderate). Since underlying cells may be affected by the specific gravity of the test sample, this practice is limited to the evaluation of cells outside the perimeter of the overlying test sample.

Table 1. Classification scheme according to the location of morphologically altered cells [47].

Grade	Reactivity	Description of Reactivity Zone
0	None	No detectable zone around or under specimen
1	Slight	Some malformed or degenerated cells under specimen
2	Mild	Zone limited to area under specimen
3	Moderate	Zone extends 0.5 to 1.0 cm beyond specimen
4	Severe	Zone extends greater than 1.0 cm beyond specimen

4) Cell Growth on Foil

To compare cell growth on a-C:H film on PEEK and PVC foil to growth on cell culture plates, foils were inserted and fixed in 6-well plates in a way that the entire well surface was covered by the foil. An amount of 250,000 MRC-5 cells were seeded in each well and cultured for 48 h. Calcein AM is a non-fluorescent cell-permeable dye, which after enzymatic cleavage by viable cells is converted to the intensely fluorescent calcein. Medium was discarded and Calcein (2 µM, Invitrogen) in fresh medium added for 30 min at RT in the dark. After washing with PBS, pictures were taken with a confocal laser scanning microscope LSM510 Meta (Zeiss). Images were acquired at 488 nm excitation wavelength using a BP 505–550 nm band-pass detection filter for the green channel (Calcein AM). Fluorescence was read at a FLUOstar Optima (BMG Labortechnik) with excitation at 485 nm and emission at 520 nm. Subsequently, cells were detached from the support and cell numbers determined using an automated cell counter based on electrochemical sensing (CasyTT, Inovatis).

2.3.6. Characterization of the Microbiological Film Properties

In order to analyze the microbiological properties of the coatings according to ISO 22196 [48], the samples were cut into 5 cm × 5 cm pieces and covered with bacterial suspension with approximately (2.5×10^5–1.0×10^6 colony forming units /mL (cfu)). The samples were incubated for 24 h at 95% relative humidity and 37 °C. Staphylococcus aureus DSM 346, DSM 799 und Escherichia coli DSM 1576 were used as bacterial strains for testing. During the incubation the bacterial suspension was covered with a 4×4 cm^2 PET foil. The used volume of the suspension should exactly wet the 4×4 cm^2 foil. Soybean Casein Lecithin Polysorbate 80 broth (SCDLP, nutrient media with Tween 80) was added for the isolation of the bacteria after the incubation. The samples were shaken for 1 min at 125 rpm and plated on Casein-Soy-Agar (CSA). To determine the starting germ numbers, the samples were directly isolated after covering.

3. Results and Discussion

3.1. Chemical Composition, Binding and Chemical Structure Analysis of the Films

The film materials, described above in Section 2.2, were chosen from chemical elements with well-known non- or low cytotoxicity (C, O, N, Ti, Si) to minimize any possible negative effects on the biological interaction. This interaction to proteins and cells occurs on the topmost surface of the material, which is generally the oxide layer formed by oxidation in ambient atmosphere after vacuum film deposition. Proofing the chemistry of this surface was carried out by surface sensitive XPS investigations (1–3 nm analysis depth) without any sputtering of the oxide surface layer. Results are shown in Table 2.

SiO_x films are slightly substoichiometric with an O/Si ratio of 1.85 (SiO_2:O:Si = 2.0) The oxygen contents of the other films were found to be between 6.5 and 32 at% leading to an O/C ratio between 0.07 and 0.53 with the highest values for the Ti doped DLC film (a-C:H:Ti) and the lower for pure, N and Si doped films. The ratio of (Si, Ti, N) dopant to carbon atoms is found to be Si/C = 0.02, N/C = 0.11, and Ti/C = 0.13 for a-C:H:Si, a-C:H:N, a-C:H:Ti films, respectively.

Table 2. Results of the chemical X-ray photo-electron spectroscopy (XPS) analysis of thin film surfaces: Binding energies, calculated element concentrations and concentration ratios.

Binding state	**SiO_x**		**a-C:H**		**a-C:H:N**		**a-C:H:Si**		**a-C:H:Ti**	
	Binding energy [eV]	Content [at%]	Binding energy [eV]	Content [at%]	Binding energy [eV]	Content [at%]	Binding energy [eV]	Content [at%]	Binding energy [eV]	Content [at%]
C1s	282.80	8.27								
	284.80	17.74	284.60	78.41	284.60	41.65	284.60	58.11	284.60	44.21
			285.54	10.59	285.57	18.69	285.62	7.71	285.90	8.50
			286.84	3.20	286.51	9.64	286.47	11.28	286.98	4.35
					287.70	4.87	287.64	5.64		
			288.31	1.30					288.41	3.24
					288.84	2.78	288.79	2.99		
					290.50	0.60				
ΣC		26.02		93.50		78.23		85.73		60.29
Si2p	100.88	4.57								
							101.16	0.35		
							102.53	1.38		
	103.43	21.40								
ΣSi		25.97						1.73		
Ti2p									458.49	6.88
									471.54	0.81
ΣTi										7.69
N1s					398.23	1.09				
					398.93	3.58				
					400.01	3.48				
					401.23	0.70				
					402.81	0.30				
ΣN						9.15				
O1s	529.16	0.76							529.92	16.44
	530.64	36.90								
			531.14	1.20	531.11	3.78	531.16	4.49	531.23	7.69
	532.16	10.34	532.13	3.40	532.25	5.37	532.2	1.50	532.14	5.67
			533.11	1.90	533.38	3.48	533.2	6.56	533.15	2.23
ΣO		48.01		6.50		12.62		12.54		32.02
x/C					N/C	0.11	Si/C	0.02	Ti/C	0.13
O/C		1.85		0.07		0.16		0.14		0.53
O/x	O/Si	1.85					O/Si	7.26	O/Ti	4.16

Comparing the peak positions of the binding energy spectra with literature data for AlKα radiation [49] allows conclusions for the formed chemical compounds: Standard bond energies for carbon (C1s) are between 280.8 and 283.0 eV for metal carbides, 284.5 eV for graphite, 285.2–288.4 eV for C–N, and 286.1–291.5 eV for C–O compounds. Thus, the films contain a high fraction of C–C bonds and only small fractions of C–O and C–N bonds. Metal carbide bonds are rather missing (e.g., being at 281.6 eV for TiC). Binding energy for Si2p is between 98.8 and 99.5 eV for pure Si, between

102.3 and 103.8 eV for SiO_2, and in between these thresholds for substoichiometric compounds. Thus, the SiO_x and a-C:H:Si film surfaces contain mixtures of Si and SiO_2 bonds with contributions of carbidic bonds in the doped DLC coating (standard binding energies for SiC: 99.9–100.9 eV). The high bond energy of the Ti2p peak indicates TiC-type bonds for the a-C:H:Ti film [50]. N1s binding energies between 398 and 403 eV give hints for N incorporation in organic matrix (399–401 eV). Low binding energies for O1s in a-C:H:Ti (528.2–531.1 eV) indicate metal oxides (e.g., TiO_2: 529.9 eV), high energies in a-C:H:Si and SiO_x (532.5–533.5 eV) SiO_2.

The structural analysis of all carbon coatings was performed by Raman spectroscopy with much lower surface sensitivity (>10 nm analysis depth) than XPS. Basis for this analysis is the frequency shift of the incident light by Raman active molecules (Stokes scattering): Amorphous carbon has five frequency shifts (bands) between 800 and 2000 cm^{-1}, of which two enable conclusions on the chemical structure: The G band around 1550 cm^{-1} is due to longitudinal oscillations of C atoms in sp^2 hybridization in rings and chains. Conversely, the D band around 1350 cm^{-1} is due to centric oscillations of C atoms in rings. The intensity ratio of these two bands (I_D/I_G) provides the basis for all estimations of the sp^2 bond content in ring structures [50]: Lower values are found for C atoms in chain structures, higher values for C in aromatic rings. If the D band is missing, no sp^2 hybridization of C in rings is present. Detailed information of the elemental bonds is gathered by FWHM analysis of the G band [51], which is influenced by the structural disorder (bond lengths and angles). High FWHM (G) is found for a-C:H with max. 30 at% H (non-polymeric films) with high C–C sp^3 hybridization.

Figure 4 shows the overview of the taken Raman spectra in the range of the significant shifts for carbon atoms, Table 3 the results of Gauss-Lorentz peak fitting (peak position FWHM, I_D/I_G ratios). The shown curves reveal an amorphous C structure for the a-C:H, a-C:H:N, and a-C:H:Ti films. However, the a-C:H:Si film is rather weak in Raman activity, which could be the reason for the high Si:C ratio. The G band is found for undoped a-C:H around 1534 cm^{-1} and increases by N and Ti doping to 1543–1544 cm^{-1}, with highest FWHM (G) found for a-C:H:N. The positions of the D band are between 1340 and 1380 cm^{-1} for a-C:H and a-C:H:N, but only at 1280 cm^{-1} for a-C:H:Ti films. No tendency in relation to the film material is found for the FWHM (being generally between 300 and 350 cm^{-1}). The smallest I_D/I_G ratio was evaluated for the a-C:H:Ti film and increases for a-C:H and a-C:H:N films, revealing a shift of carbon binding from chain to aromatic ring structures. The higher FWHM (G) of a-C:H:N leads to expect a higher sp^3 content in C–C bonds.

Table 3. Calculated wave numbers of peak maxima and FWHM (full width at half maximum) values of the D and G bands as well as I_D/I_G ratio of all diamond-like carbon based materials (DLC) films with measurable peaks (a-C:H, a-C:H:N, a-C:H:Ti) .

Film type	D [cm^{-1}]	FWHM (D) [cm^{-1}]	G [cm^{-1}]	FWHM (G) [cm^{-1}]	I_D/I_G [1]
a-C:H	1345.26	324.25	1534.46	194.48	0.42
a-C:H:N	1377.09	332.49	1543.53	172.99	0.76
a-C:H:Ti	1277.10	291.01	1542.76	180.40	0.31

Figure 4. Raman shifts of the carbon based thin films (a-C:H, a-C:H:N, a-C:H:Si, a-C:H:Ti) in the characteristic wave number range for the D (1350 cm^{-1}) and G band (~1550 cm^{-1}) of carbon.

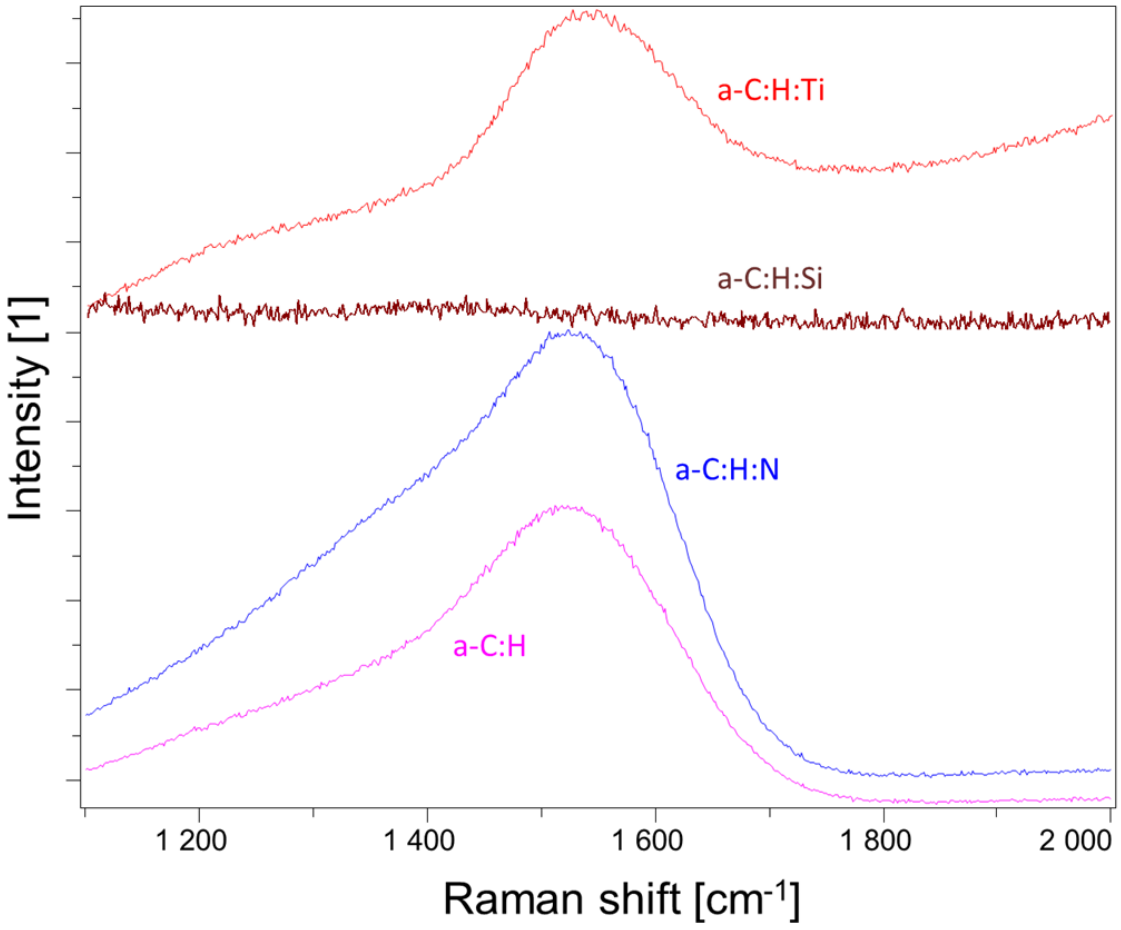

3.2. Growth Structures and Phase Compositions of the Films

The investigation of the film structure with high resolution microscopy (HR-TEM) and electron diffraction (SAED) show a large content of amorphous matrix in the micro- and nanostructures of the films (a-C:H: Figure 5a, a-C:H:Si: Figure 5b). Similar results can be expected for SiO_x films [52]. Partly nanocrystalline contents are only found for a-C:H:Ti films (Figure 5c), containing TiC nano-grains (5–10 nm diameter) in an amorphous C matrix. These results were obtained by studying films of 500 nm thickness on silicon wafer substrates, because HR investigations of ultra-thin films on polymers are rather impossible. Based on earlier works [53], the crystallinity on polymer substrates is generally lower than on Si due to effects in film growth (see description below). Compared to the size of focal adhesions (>500 nm diameter) providing the strong adhesion of cells on surface, the size of these nano-grains are extremely small.

Figure 5. High resolution microscopy (HR-TEM)images of (**a**) a-C:H, (**b**) a-C:H:Si, and (**c**) a-C:H:Ti films with >500 nm thickness on Si substrates. Electron diffraction (SAED) reveals an amorphous structure for a-C:H:Si (b), but a nanocrystalline structure for a-C:H:Ti (cubic TiC precipitations).

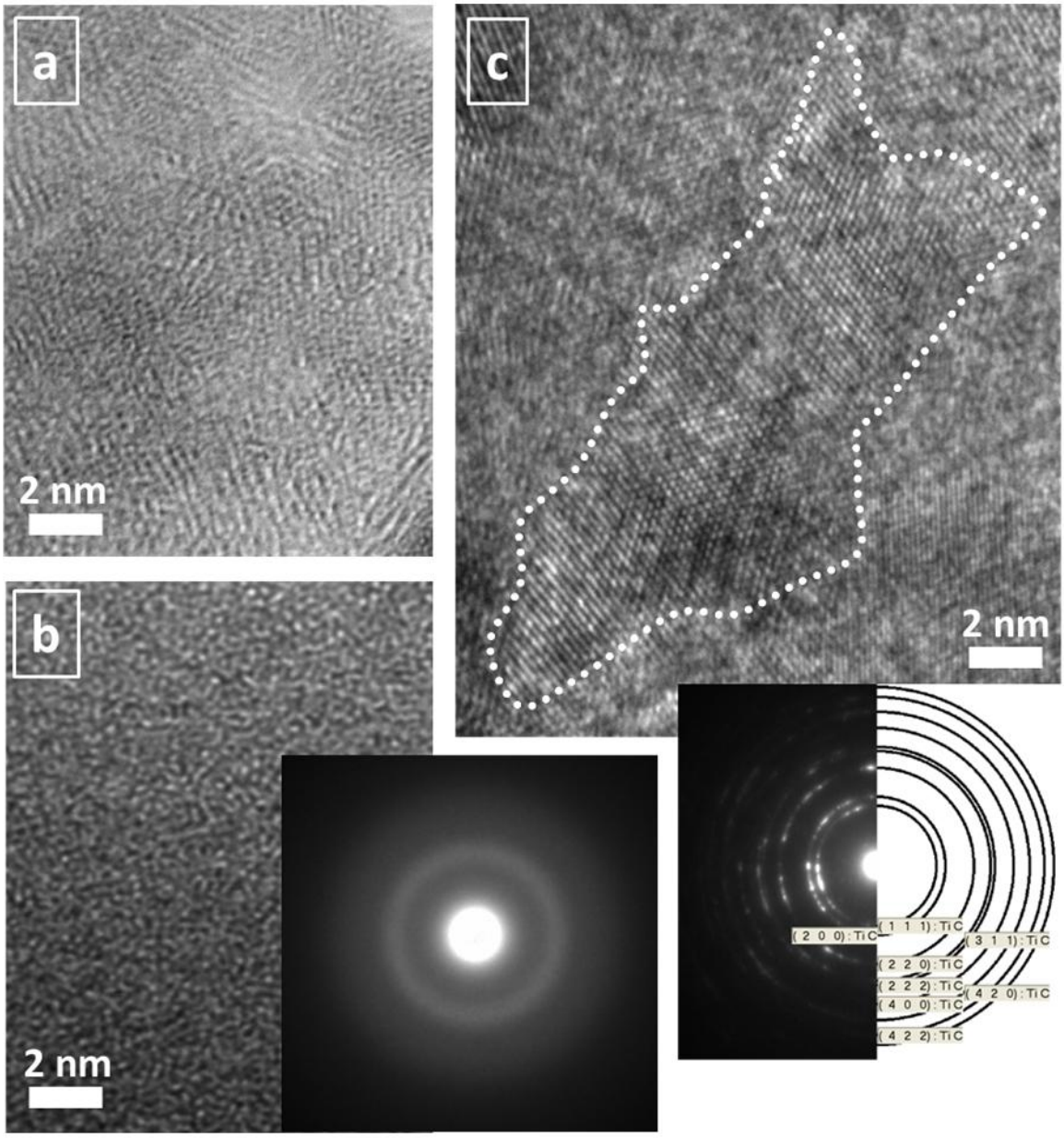

3.3. Film Topography on the Micro- and Nanometer Scale

Nano- and micro-sized defects in the films have especially a decisive influence on the gas barrier behavior. Consequently, strong attention was paid to topographical imaging: Light microscopy images in Figure 6 show the topography on the micrometer scale of the films on PEEK as well as of the uncoated PEEK as reference. In contrast to the homogenous appearance of the PEEK substrate surface under the light microscope in reflected-light mode (Figure 6a), the deposited films (Figure 6b–f) possess distinct topographical features: This black-white contrast, indicating different intensity of reflected light by variously aligned surfaces, is significantly larger in the case of DLC based materials

(a-C:H, a-C:H:N, a-C:H:Si, and a-C:H:Ti) than for SiO_x. Furthermore, these topographical structures are finer for ion source deposited than for sputtered films. Microdefects like pinholes, particulates, droplets, *etc*. are missing rather: Counting of light microscopically visible defects (>1 μm diameter) on 1 mm^2 large areas reveals 5 ± 1 mm^{-2} for a-C:H:Ti, 6 ± 1 mm^{-2} for a-C:H:Si, 10 ± 1 mm^{-2} for a-C:H:N, 19 ± 2 mm^{-2} for SiO_x, and 21 ± 2 mm^{-2} for a-C:H films. In contrast to our expectations, the magnetron sputtered films contain significantly less defects than the ion source deposited.

Figure 6. Light microscopical images of (**a**) uncoated polyetheretherketone (PEEK) and thin films of 26 ± 3 nm on PEEK: (**b**) SiO_x; (**c**) a-C:H; (**d**) a-C:H:N; (**e**) a-C:H:Si; and (**f**) a-C:H:Ti.

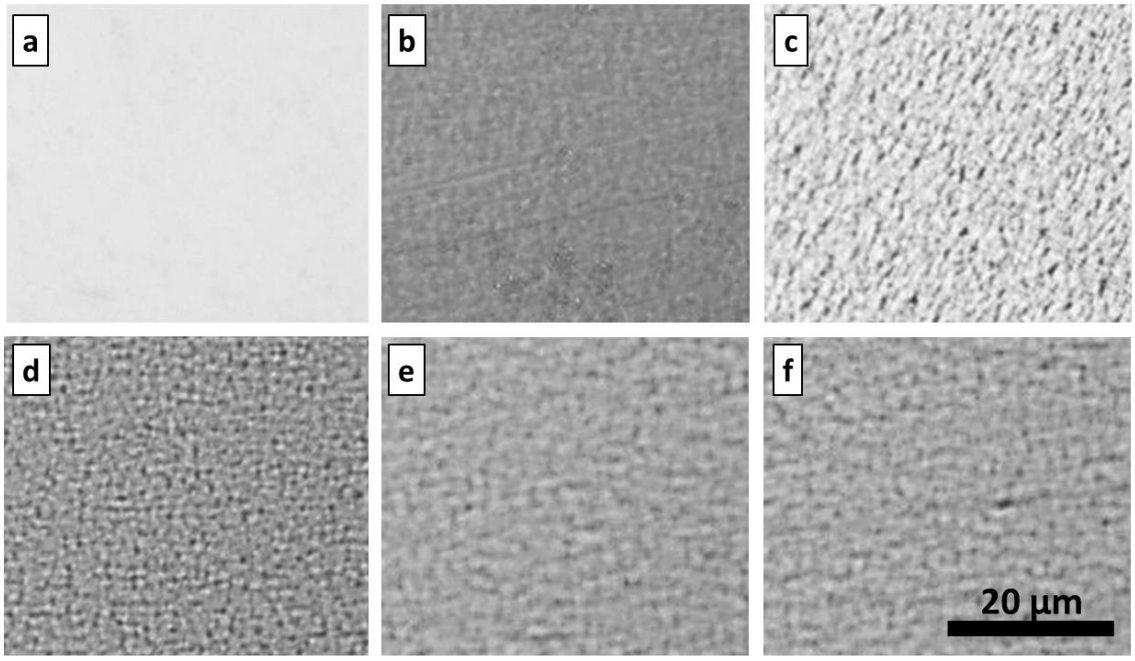

Detailed investigations of the surface nanotopography were carried out by AFM: Images are shown in Figure 7 for films on PEEK and for comparison and for discussion of the occurring growth phenomena in Figure 8 for films on glass substrates. Calculated RMS roughness, lateral correlation length (LCL), and Hurst parameter values are given in Table 4. RMS roughness, a measure of the vertical roughness, provides height (amplitude) information of the topographical features, while LCL data indicates lateral frequency of the roughness features (lateral distance, across which heights of the surface are correlated).

Generally, the several times smoother glass substrate results in smaller RMS roughness, standard deviation of RMS, and LCL of the thereon deposited films compared to films on PEEK. Furthermore, no significant differences are found for RMS and LCL data obtained from 2 × 2 and 16 × 16 μm^2 images on glass. However, the image size strongly influences these values for coated and uncoated PEEK. In contrast, a significant influence of the Hurst parameter, describing the "jaggedness" of the surface, is missing for differently sized images obtained from coated PEEK, but found for films on glass substrates. Generally, films deposited on glass substrates exhibited a smoother topography, resulting in smaller RMS. The smoothest film is found to be the ion source deposited a-C:H, the roughest the sputtered SiO_x and a-C:H:Si. For the latter film, the LCL is also quite high, which is due

to some large features influencing the data analysis. The images (Figure 8b–f) reveal preferentially filling of the valleys in between the roughness tips of the uncoated glass substrate (Figure 8a) with material during deposition by diffusion. Due to room temperature deposition, diffusion is scarcely thermally activated and needs additional driving force, provided by higher energetic species from the plasma. While the ion energy during (non-biased) DC pulsed or RF sputtering is generally lower than 20 eV, ions and kinetic atoms in the fragmented ethyne precursor plasma have several 100 eV of energy (medium energy ~400 eV). Reasonably, the ion source deposited a-C:H and a-C:H:N films are decisively smoother than all others. This is visible in Figure 8c,d which also lack the dot-like features of about 20 nm lateral size and 30–50 nm distance (LCR) , which are found for a-C:H:Si, a-C:H:Ti and SiO_x (Figure 8b,e,f). Such features have been widely studied for crystalline thin film growth and are due to the preferred growth of some crystallographically well aligned nano-grains. For preponderant amorphous films on not ultra-smooth substrates, this process is influenced by the substrate topography.

Figure 7. Atomic Force Microscopy (AFM) surface topography images of (**a**) PEEK substrate, and (**b**) SiO_x, (**c**) a-C:H, (**d**) a-C:H:N, (**e**) a-C:H:Si, and (**f**) a-C:H:Ti on PEEK substrates. (image size: 2 × 2 μm^2, height scale: 100 nm)

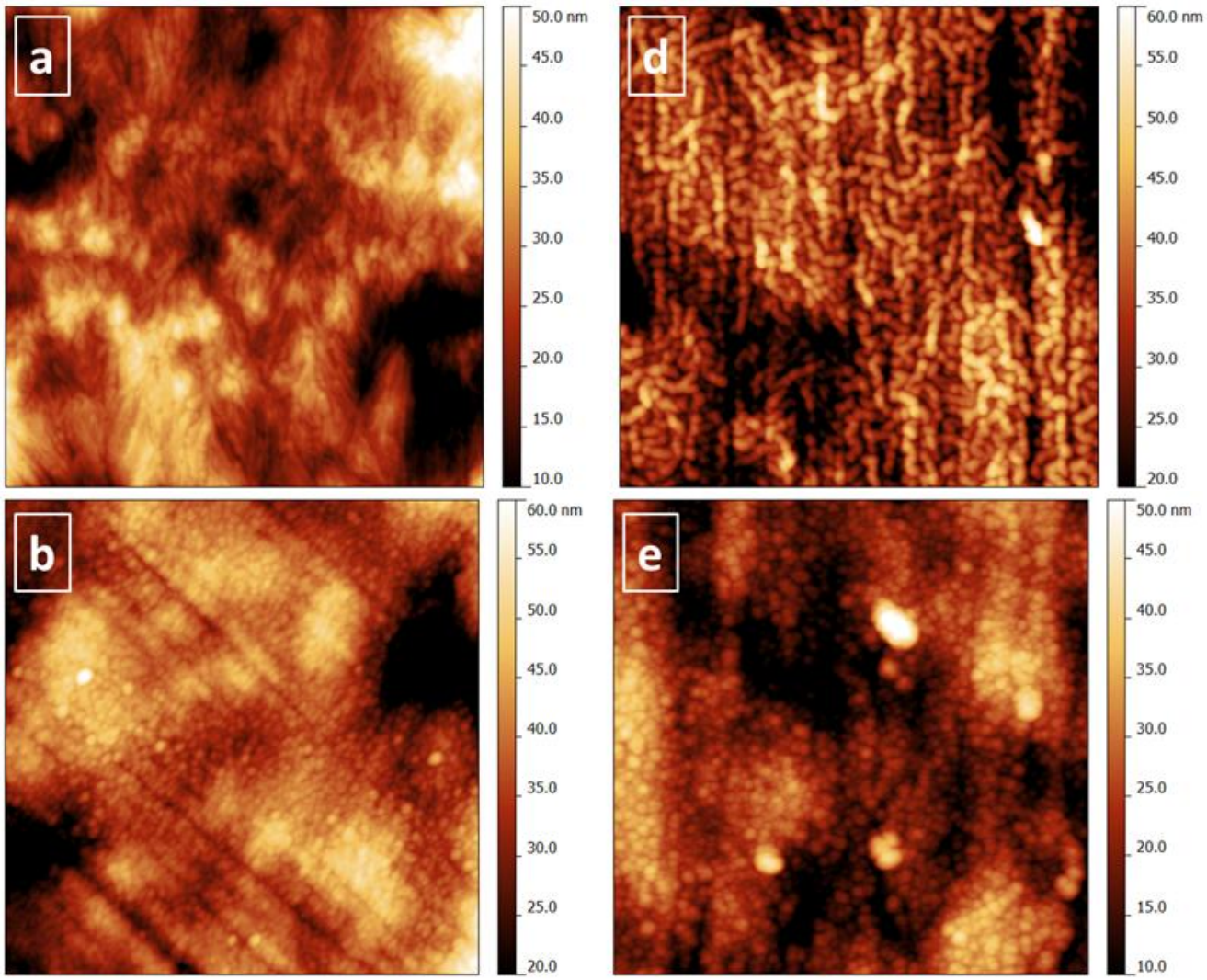

Figure 7. *Cont.*

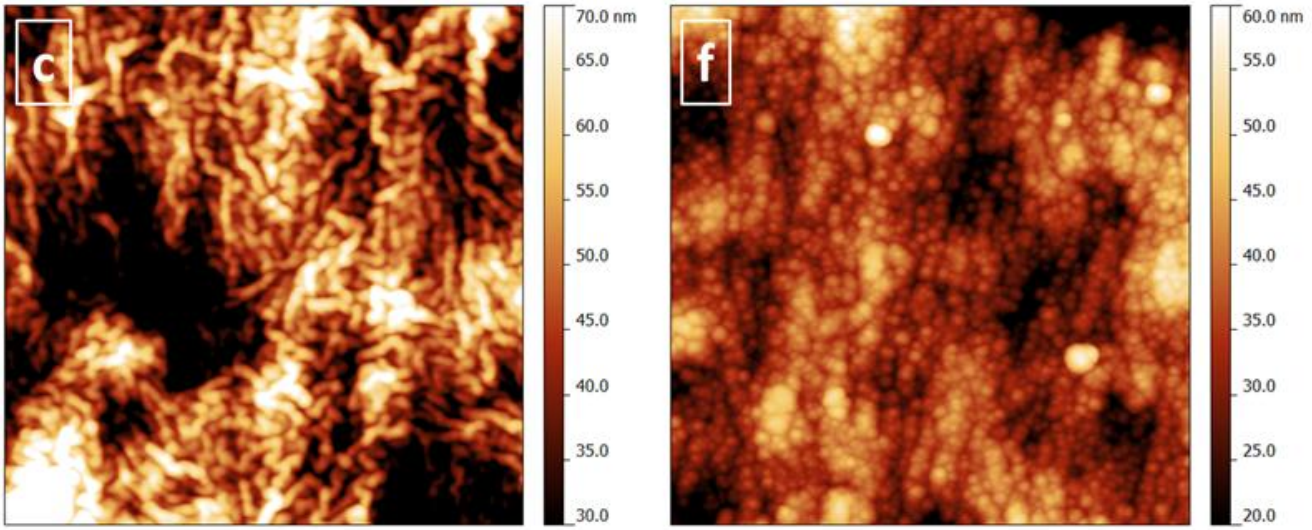

Figure 8. AFM surface topography images of (**a**) glass substrate, and (**b**) SiO_x, (**c**) a-C:H, (**d**) a-C:H:N, (**e**) a-C:H:Si, and (**f**) a-C:H:Ti on glass substrate. (image size: 2 × 2 μm^2, height scale: 30 nm)

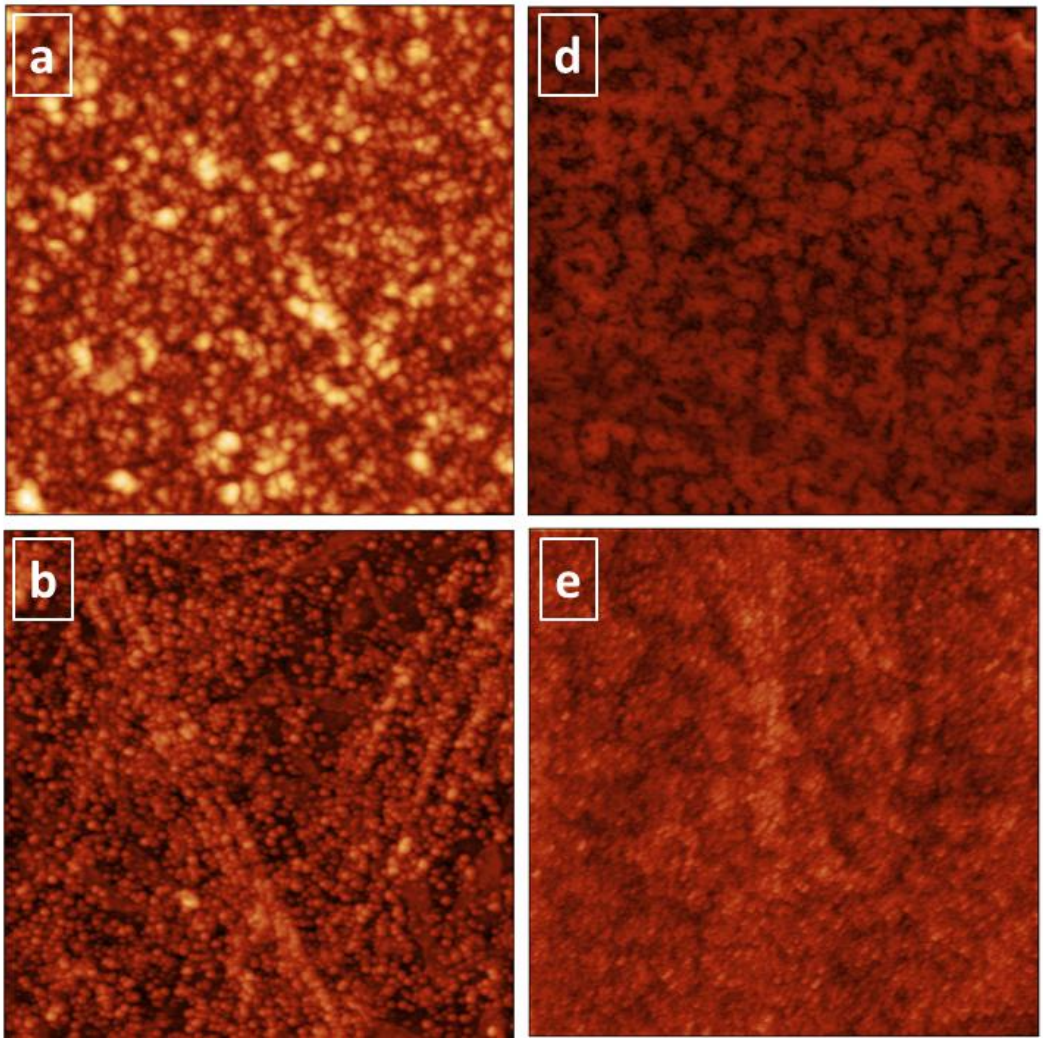

Figure 8. *Cont.*

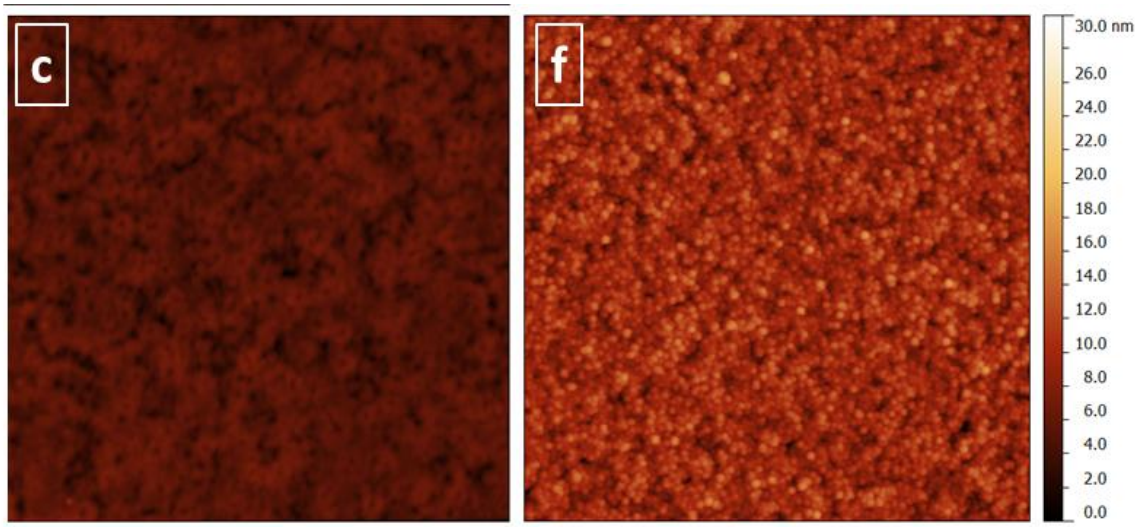

Table 4. Root-mean-squared (RMS) roughness, lateral correlation length and Hurst parameter of uncoated substrates (PEEK, glass) and ~25 nm thin films thereon.

Material			Substrate	SiO_x	a-C:H	a-C:H:N	a-C:H:Si	a-C:H:Ti
PEEK	RMS roughness [nm]	16 × 16 µm² scan size	26.70 ± 4.85	22.85 ± 2.70	25.70 ± 1.05	25.15 ± 3.45	19.05 ± 1.65	24.05 ± 1.45
		2 × 2 µm² scan size	9.50 ± 1.05	8.60 ± 0.70	13.65 ± 2.35	8.70 ± 0.60	7.50 ± 0.65	9.35 ± 1.85
	Lateral correlation length ξ [nm]	16x16 µm² scan size	1200 ± 600	1100 ± 150	1200 ± 250	1600 ± 250	1100 ± 150	745 ± 85
		2 × 2 µm² scan size	220 ± 40	260 ± 50	170 ± 45	130 ± 45	200 ± 60	220 ± 60
	Hurst parameter α [1]	16 × 16 µm² scan size	0.55 ± 0.10	0.60 ± 0.05	0.50 ± 0.00	0.50 ± 0.05	0.50 ± 0.05	0.50 ± 0.00
		2 × 2 µm² scan size	0.80 ± 0.20	0.70 ± 0.10	0.50 ± 0.05	0.50 ± 0.00	0.60 ± 0.10	0.55 ± 0.05
Glass	RMS roughness [nm]	16 × 16 µm² scan size	4.55 ± 1.20	2.75 ± 0.20	1.15 ± 0.25	1.95 ± 0.40	2.10 ± 1.25	2.10 ± 0.10
		2 × 2 µm² scan size	3.85 ± 0.55	2.75 ± 0.15	0.80 ± 0.10	1.80 ± 0.20	3.40 ± 2.40	2.10 ± 0.15
	Lateral correlation length ξ [nm]	16 × 16 µm² scan size	80 ± 55	80 ± 25	155 ± 120	125 ± 65	160 ± 65	40 ± 5
		2 × 2 µm² scan size	45 ± 5	30 ± 10	35 ± 5	40 ± 5	140 ± 100	20 ± 1
	Hurst parameter α [1]	16 × 16 µm² scan size	0.65 ± 0.10	0.50 ± 0.00	0.50 ± 0.00	0.55 ± 0.05	0.55 ± 0.05	0.65 ± 0.05
		2 × 2 µm² scan size	0.85 ± 0.05	0.70 ± 0.05	0.80 ± 0.10	0.75 ± 0.05	0.60 ± 0.10	0.85 ± 0.05

On PEEK substrates, the film formation mode appears to be very different especially for a-C:H and a-C:H:N, if comparing to layers on glass substrate: Apart from the overall rougher topography of PEEK, the growth mode of sputtered films appears to be similar to glass with the formation of small dots. Compared to the substrate, the RMS and LCL are not significantly influenced. a-C:H and a-C:H:N films form a different type of topography, consisting of worm-like features. Such a film formation process ("nano-wrinkling") was described by the authors for other soft polymer substrate types [54–56] and is mechanically influenced: The higher the energy of the deposited species, the higher is the tendency to implantation of plasma species into the growing films. Such a several nanometer deep implantation increases the intrinsic stresses of the films. Soft substrates like polymers are able to deform elastically to decrease the intrinsic stress, which is generally compressive under the applied deposition conditions. The result of this stress relaxation is the tensile straining of the surface, resulting in a wavy topography. Stress relaxation occurs stepwise in continuing film growth: Thicker films on polymers are stiffer and, thus, wrinkle to reduce the internal stress at larger wavelengths. Finally, a hierarchically self-structured surface is formed. While a 25 nm film thickness is sufficient on a soft PU substrate (E < 0.5 GPa) for the introduction of a second, larger hierarchical wrinkle structure, such topography is not incisive on PEEK (E ~ 2.5 GPa).

3.4. Mechanical Behavior of Films—Elastic Modulus and Hardness

Indentation tests were used to obtain the mechanical properties of the thin films. To exclude influences of soft substrate deflection under the applied measurement loads, >500 nm thick films on silicon substrates were applied with >1 mN normal forces on the Berkovich indenter to guarantee a maximum indentation depth of 10% of the film thickness and to measure intrinsic film properties. However, this excludes the compound properties and, thus, the influences of wrinkling on elastic properties. Generally, wrinkles smooth out under tensile stresses, providing higher total substrate strain to film failure [57]. However, studies which included such substrate material behavior (thus, giving information about the compliance of substrate and film) were previously published by the authors [58]).

Calculated hardness and elastic modulus data from thick films, based on Oliver-Pharr [36] theory, are shown in Table 5. Although these mechanical values were gathered from measurements on silicon substrates, they provide the basis for a qualitative discussion and allow predictions of the behavior of coated polymers. Elastic deformability is of general importance in the field of "stiff" and dense gas permeation barrier of thin film materials on soft, deformable polymers: Cracks under tensile stresses, which develop during bending of the very thin foil substrates, must also be prevented. Elastic modulus and hardness give measures of the dependency of stress and strain in the elastic regime and for the ultimate strength before plastic deformation (the end of the elastic regime), respectively. In combination, the ratio H/E (elasticity ratio) provides a factor to compare materials [59,60]: A high elasticity ratio indicates high elastic deformability before fracture. As visible in Table 5, non-wrinkled a-C:H:Si as well as SiO_x thin films on stiff Si substrates would be the best candidates based on the H/E ratio. Values for fracture toughness (K_c) based on crack propagation after Vicker indentation [37,38] are also given in Table 5, which give an indication of the plastic deformability of the material before the onset of fracture: High values are present for nanocrystalline a-C:H:Ti films.

Table 5. Hardness (*H*), elastic modulus (*E*), fracture toughness (K_c) and elasticity ratio (*H*/*E*) of >500 nm thick coatings on Si substrates.

Coating type	*H* [GPa]	*E* [GPa]	K_C [MPa $m^{0.5}$]	*H*/*E* [1]
a-C:H	18.5 ± 2.2	206 ± 16	0.9 ± 0.1	0.0898
a-C:H:N	14.2 ± 1.9	163 ± 8	1.1 ± 0.1	0.0871
a-C:H:Si	18.0 ± 2.1	170 ± 6	1.6 ± 0.1	0.1059
a-C:H:Ti	18.6 ± 2.2	260 ± 15	3.9 ± 0.2	0.0715
SiO_x	7.9 ± 1.3	75 ± 3	0.7 ± 0.1	0.1056

3.5. Wetting Characteristics and Surface Energies of the Films

The wetting behavior as well as the surface energy of the coatings was characterized by contact angle measurements with 1 µL droplet size, followed by Kaelble plotting for calculating the polar and dispersive contributions to the surface energy (Table 6). Basically all films as well as the PEEK substrate are hydrophobic with the lowest water contact angle found for SiO_x. While the PEEK substrate and the carbon based films have a high dispersive contribution to the total surface energy, the polar contribution is significantly higher for the SiO_x films. The highest total surface energy is present for a-C:H:Ti, followed by SiO_x films, while all other materials show rather similar, lower values. Comparing these results with the chemical composition on the surface, the high oxygen content on the a-C:H:Ti film by the atmospheric oxidation reaction of Ti seems to be the cause of this behavior.

Table 6. Contact angles and surface energies (total, polar, dispersive) of PEEK foils and thin films on PEEK.

Material	PEEK	SiO_x	a-C:H	a-C:H:N	a-C:H:Si	a-C:H:Ti
$H_2O^{deionized}$ contact angle [°]	85.2 ±3.0	48.8 ± 2.8	92.9 ± 1.0	95.3 ± 0.8	88.3 ± 1.6	108.5 ± 0.8
Polar contribution to surface energy σ_s^p [mJ m^{-2}]	3.5	37.9	1.3	0.7	3.1	1.0
Dispersive contribution to surface energy σ_s^d [mJ m^{-2}]	33.3	11.3	36.2	39.3	33.8	57.5
Total surface energy σ_s [mJ m^{-2}]	36.8	48.98	37.5	40.0	36.9	58.5

Contact angle measurements with about one order of magnitude smaller droplet size (one picoliter, average lateral droplet diameter in µm range) revealed in earlier investigations a significant influence of wrinkling nanotopography: While thicker films with 100 nm are highly hydrophobic (contact angle of a-C:H and titanium nitride on polyurethane ~80 °), such films of 20 and 23 nm thickness with only first order wrinkles (~26 nm RMS, similar to results of this work) are significantly higher hydrophilic (water contact angle ~50 °).

3.6. Gas Permeation Behavior

The permeation of O_2 through coated as well as uncoated PEEK was measured by optochemical analysis. Presented data for the OTR in Table 7 indicates very high oxygen permeation through the 50 µm thick PEEK foil (>200 cm^3 m^{-2} d^{-1} bar^{-1}, being out of the range of the highly accurate analysis technique). Even 26 nm thin films reduce the oxygen permeation by nearly two orders of magnitude

with high reproducibility (low standard deviation in measurements): Lowest OTR values are found for the films grown by direct ion source deposition (a-C:H, a-C:H:N), while sputtered films enable higher gas permeation. The barrier effect is higher for a-C:H:Si than for the SiO_x and a:C:H:Ti films, whereby the level of permeation is comparable to published data of sputtered oxide coatings of similar thickness [61].

Table 7. Oxygen transmission rates (OTR) of uncoated and 25 nm thin coating on PEEK.

Material	PEEK-Substrate	SiO_x	a-C:H	a-C:H:N	a-C:H:Si	a-C:H:Ti
OTR $[cm^3\ m^{-2}\ d^{-1}\ bar^{-1}]$	>200	7.91 ± 0.011	5.0 ± 0.005	3.16 ± 0.006	6.59 ± 0.016	9.74 ± 0.021

Gas permeation can be theoretically described based on the equation

$$\frac{h}{P} = \frac{h_c}{P_c} + \frac{h_s}{P_s} \quad (2)$$

in which h is the thickness and P the permeability of the film (c), substrate (s) and the whole system [62]. Generally, permeation in thin film materials is defect controlled, while the intrinsic permeation rates of the material has inferior contribution. Different effects occur for micro and nano scale defects: Pores (pinholes) and cracks with lateral size >1 µm belong to the group of micro defects [63,64], while the group of nano defects contain specific film growth effects like the porosity around the tapered grains [65]. Although the nuclei density at the beginning of film growth is about $2\ nm^{-2}$, the preferential growth of some crystals as well as the mechanical stress relaxation by wrinkling, results in the structures shown in the AFM images above (Figures 7 and 8). The effect of nano defects is much higher than that of micro defects due to their extremely high density over the whole surface. This explains the advantageous behavior of the films, deposited directly from the ion source plasma, compared to the sputtered types, although especially the a-C:H films contain a larger density of micro defects (see light microscopy results above). The OTR values for a-C:H:Si, a-C:H:Ti, and SiO_x films with lower defect density, but domed surfaces are significantly higher. A positive influence seems to occur with wrinkling, which increases the mechanical tensile strain of fracture: Before fracture, wrinkles will smooth out and form a flat surface, providing up to 5% elasticity [57]. The highest OTR value for a-C:H:Ti can both be influenced by the low elasticity index of this material and the quite porous structure (see above).

3.7. In Vitro *Biocompatibility Testing*

Although all materials in the investigations were selected from the group of non-toxic elements, biocompatibility tests were performed to finally check the interaction of the films with biological material.

In vitro testing of biomaterials based on ISO 10993 [66] requires detection of bacterial contamination and the identification of possible cellular damage as the initial steps in proof of the biocompatibility. Endotoxin from gram-negative bacteria is the most common cause of toxic reactions resulting from the contamination of pharmaceutical products with pyrogens. Their pyrogenic activity is much higher than that of most other pyrogenic substances. In spite of some pyrogens with different

structures, the absence of bacterial endotoxins in a product implies the absence of pyrogenic components, being a justified conclusion of such investigations. For the detection of endotoxin the increase in the rectal temperature of white rabbits after intravenous injection of samples extracts can be used. An alternative *in vivo* assay, the Limulus Amebocyte Lysate (LAL) assay, has replaced this assay and is recommended by the European Medicines Agency to evaluate medical devices for bacterial endotoxins [67]. The LAL test is based on the activation of coagulase in the blood cells (amoebocytes) of the horseshoe crab and was described as equivalent to the rabbit pyrogen test by Ronneberger [68]. In order to perform the bacterial endotoxins test, an aqueous extract of the sample is used as the test solution [47].

As the second step, *in vitro* cytotoxicity screening is recommended to determine the cytotoxic potential of new materials or formulations for possible use in medical applications. This is needed because any local leakage of toxic substances can result in cell damage and death, which will result in the recruitment of a variety of cells to the site of implantation. Continuous or prolonged leakage of toxic substances will induce persistent inflammation and, thereby, interfere with the successful performance of the implant. Cytotoxicity testing on cell lines shows in many cases good correlation with animal assays. It is frequently more sensitive than animal studies and equally predictive for acute toxicity in humans to rodent *in vivo* studies [69]. According to ISO 10993-5, cytotoxicity testing should be performed by eluate testing and by direct contact testing [70]. Cytotoxicity screening tests of the eluates are based on the determination of the total amount of proteins, DNA, cell number or enzymatic activity of a cell population [71]. The use of formazan bioreduction for the assessment of cell viability is a generally accepted technique [72].

The evaluation of the direct contact between cells and biomedical devices such as implants identifies the presence of potential leachables, which may induce toxic results *in vitro*. The detection of cell damage is performed by cell staining using colorimetric dyes. The cell morphology and cell detachment are recorded after 24 h exposure [45].

In pilot experiments, biocompatibility of the bare PEEK was assessed. Eluates from the foil did not decrease cell viability compared to cells treated with cell culture medium only. Viabilities were 103% ± 6% after 24 h, 102% ± 2% after 48 h, and 100% ± 9% after 72 h. Thereafter, PEEK with films were evaluated. All test sample extracts did not induce clotting of amoebocyte lysate. This indicates endotoxin levels below the detection threshold of the assay (0.06 EU/mL). Such low levels of endotoxin are regarded as non-pyrogenic according to the guidelines of the FDA and EMA [73]. Testing of eluates/extracts decreased cell viability only in the positive controls (20 nm plain polystyrene particles) but not in the samples (Figure 9, reaction of MRC-5 is shown as example). No time dependent decrease in viability was seen. Cells detached from the plastic support after exposure to the positive control (copper foil) (Figure 10, MRC-5 cells shown). Negative control and test samples showed cell loss only beneath the contact zone with the test samples. This effect is usually explained by mechanical damage. Since cells and samples are only in loose contact, additional effects by lack of oxygen or medium supply can be disregarded. Figures 11 and 12 show the different morphological features of MRC-5 and L929 cells. MRC-5 cells show the typical elongated, spindle-shaped morphology of differentiated fibroblasts (Figure 11), while the shape of L929 cells is more epitheloid (Figure 12). Both cell lines reacted to the exposure with the test samples in a similar way. In cells exposed to negative control and test samples (a-C:H foil is shown as example), the typical morphology

of the cells is maintained (Figures 11a,b,e,f and 12a,b,e,f), while cells exposed to positive control have an altered morphology with rounding and partial detachment of cells and loss of the typical nuclear architecture (Figures 11c,d and 12c,d). To find out whether cellular adherence and growth pattern on a-C:H film on PEEK, on PVC foil (non-toxic negative control), and on cell culture plates were similar, fluorescence of Calcein staining was documented and quantified, and total cell number were determined. Cells on all substrates showed strong fluorescence (Figure 13). Calcein fluorescence of cells grown on a-C:H film on PEEK and on PCV foil were 104.5% and 70.8% of control, respectively. Cell numbers on a-C:H film on PEEK and on PCV foil were 79.1% and 50.1% of control, respectively.

Figure 9. Viability of human (MRC-5) fibroblasts according to formazan bioreduction after 24 h, 48 h and 72 h in the presence of positive control (PC) and test samples (pure eluates). Marked decrease in viability is seen after exposure to the positive control (20 nm plain polystyrene particles), while no decrease in viability occurred after exposure to eluates of test samples. Cells treated with medium only are set as 100% viability.

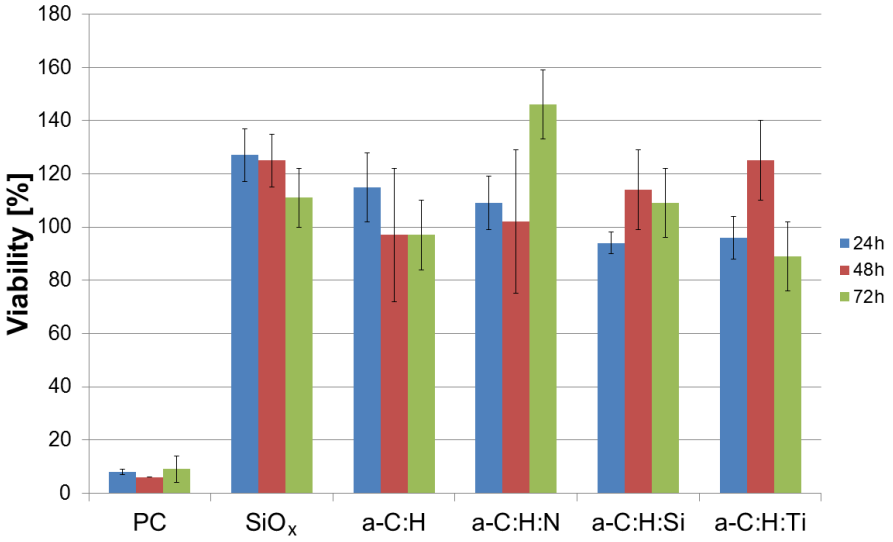

Figure 10. Crystal violet staining of MRC-5 cells (**a**,**d**) without exposure (growth control) and (**b**) after exposure to positive control, (**c**) negative control, PEEK foils with (**e**) a-C:H films and (**f**) a-C:H:N films.

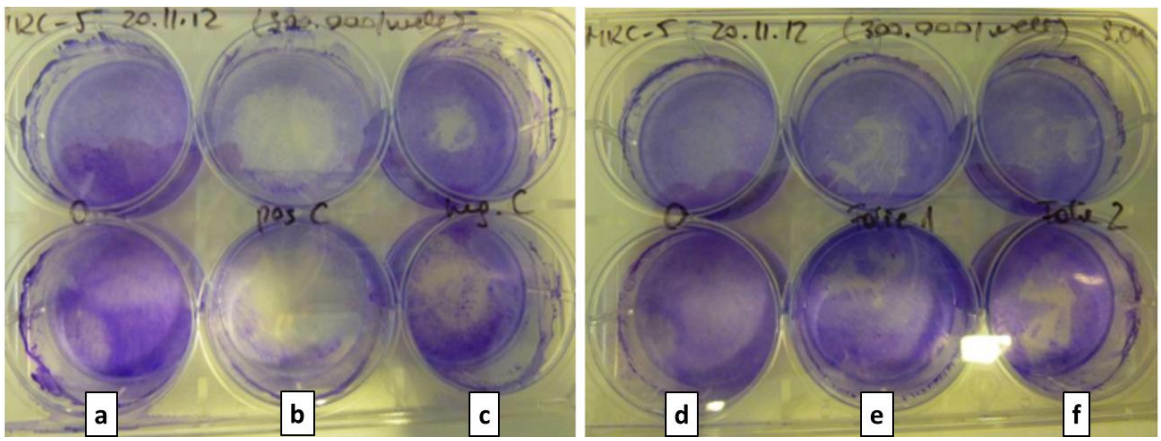

Figure 11. Human (MRC-5) fibroblasts exposed to (**a**,**b**) negative control (PVC foil), (**c**,**d**) positive control (copper foil) and (**e**,**f**) a-C:H film on PEEK. Healthy MRC-5 cells are spindle-shaped and nuclei usually containing 1–2 darker nucleoli are clearly visible (arrowheads). No morphological alterations and no detached cells are seen in cells exposed to negative control (**a**,**b**) and test sample (**e**,**f**). Cells after exposure to the positive control show rounded appearance and no normal nucleus can be discerned (**c**,**d**).

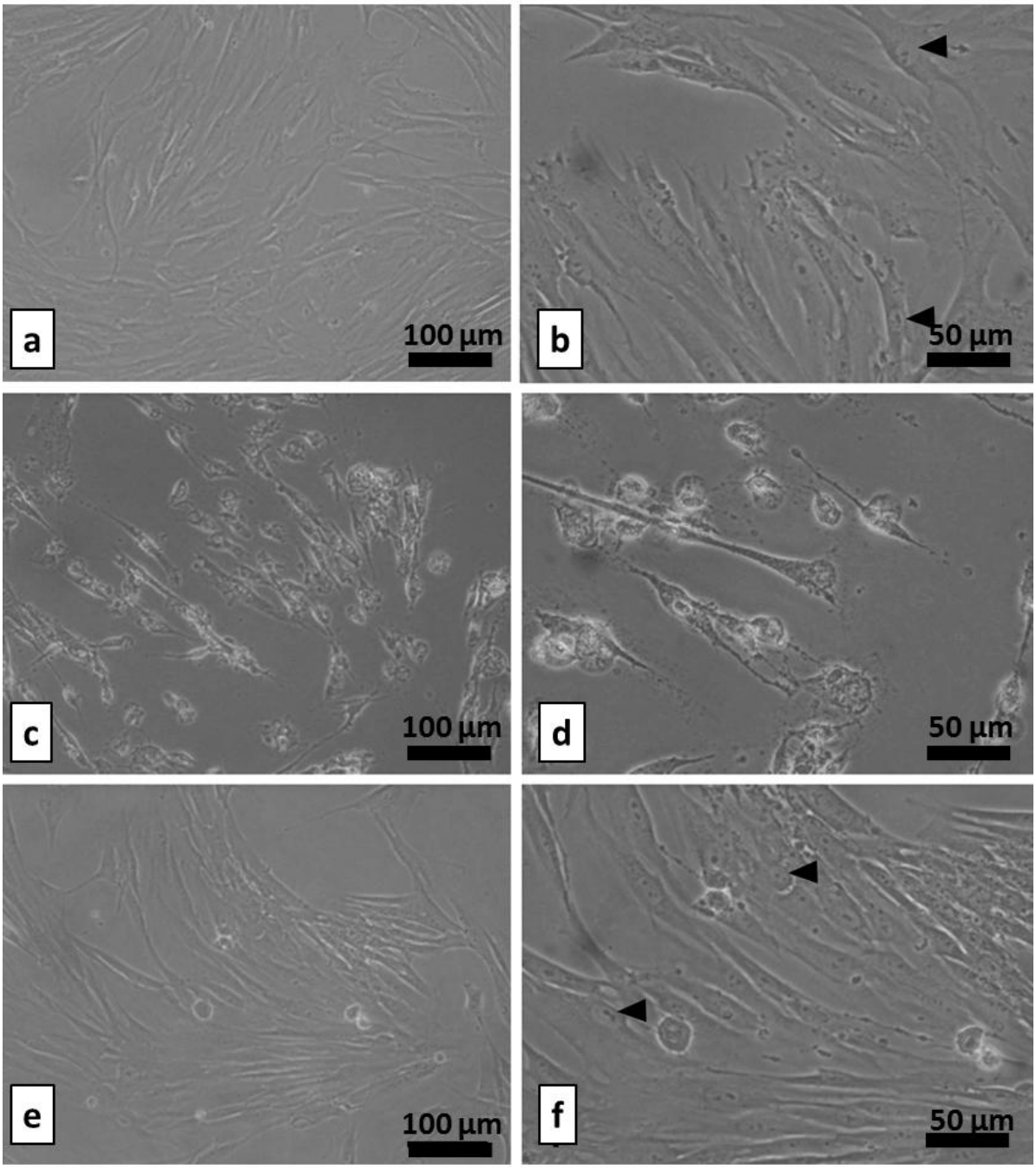

Figure 12. Murine (L929) fibroblasts exposed to (**a**,**b**) negative control (PVC foil), (**c**,**d**) positive control (copper foil) and (**e**,**f**) a-C:H film on PEEK. Healthy L929 cells at low cell density have an elongated shape and at higher densities are cuboid. Nuclei containing several nucleoli are clearly visible (arrowheads). No morphological alterations and no detached cells are seen in cultures exposed to negative control (**a**,**b**) and test sample (**e**,**f**) and occasional dividing cells are seen (arrows). Cells after exposure to the positive control show rounded appearance and no normal nucleus can be discerned (**c**,**d**).

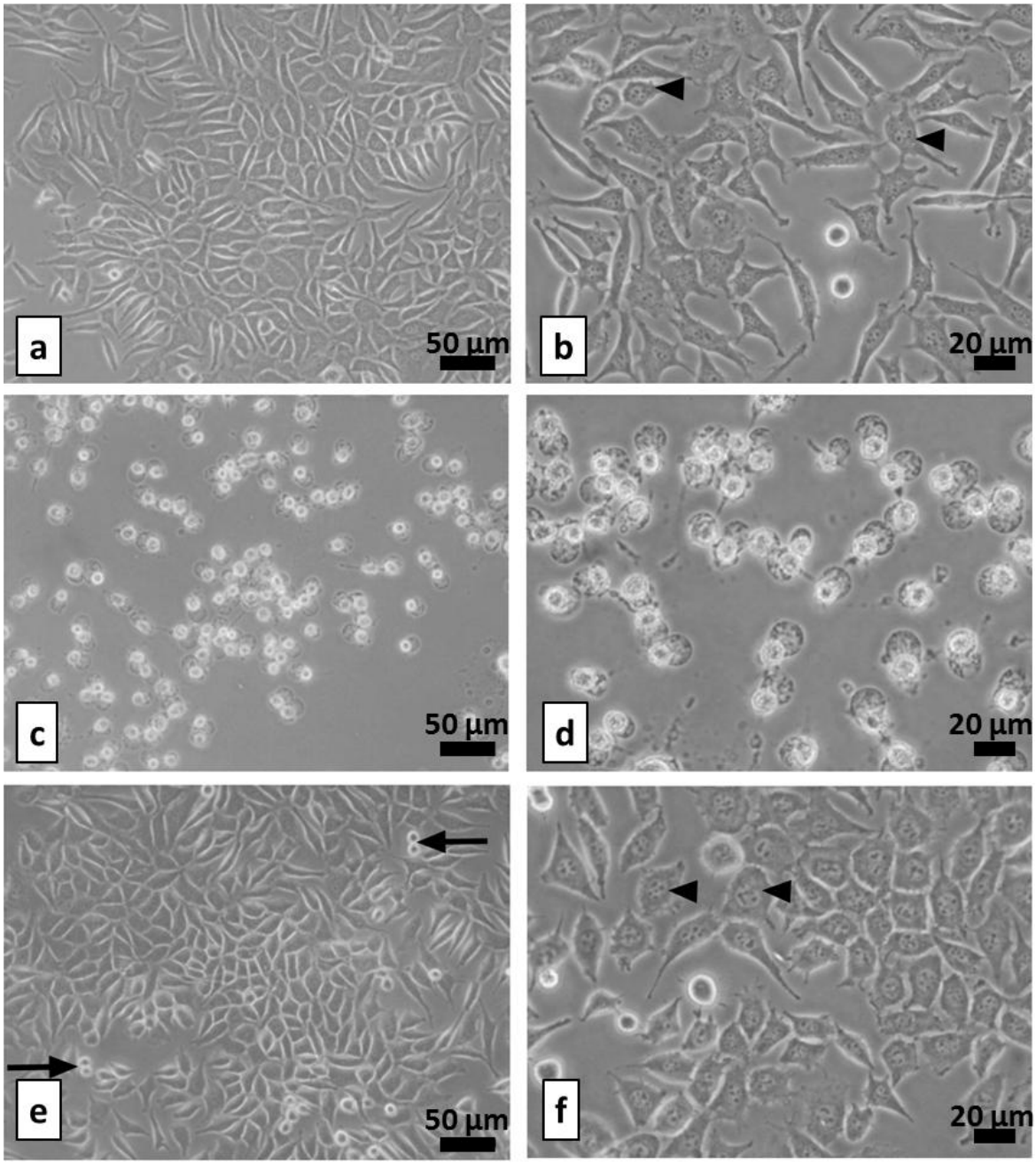

Figure 13. MRC-5 fibroblasts cultured on cell culture plate (**a**), negative control (PVC foil, **b**) and a-C:H film on PEEK (**c**) and stained with Calcein AM dye (green). Scale bar: 50 µm.

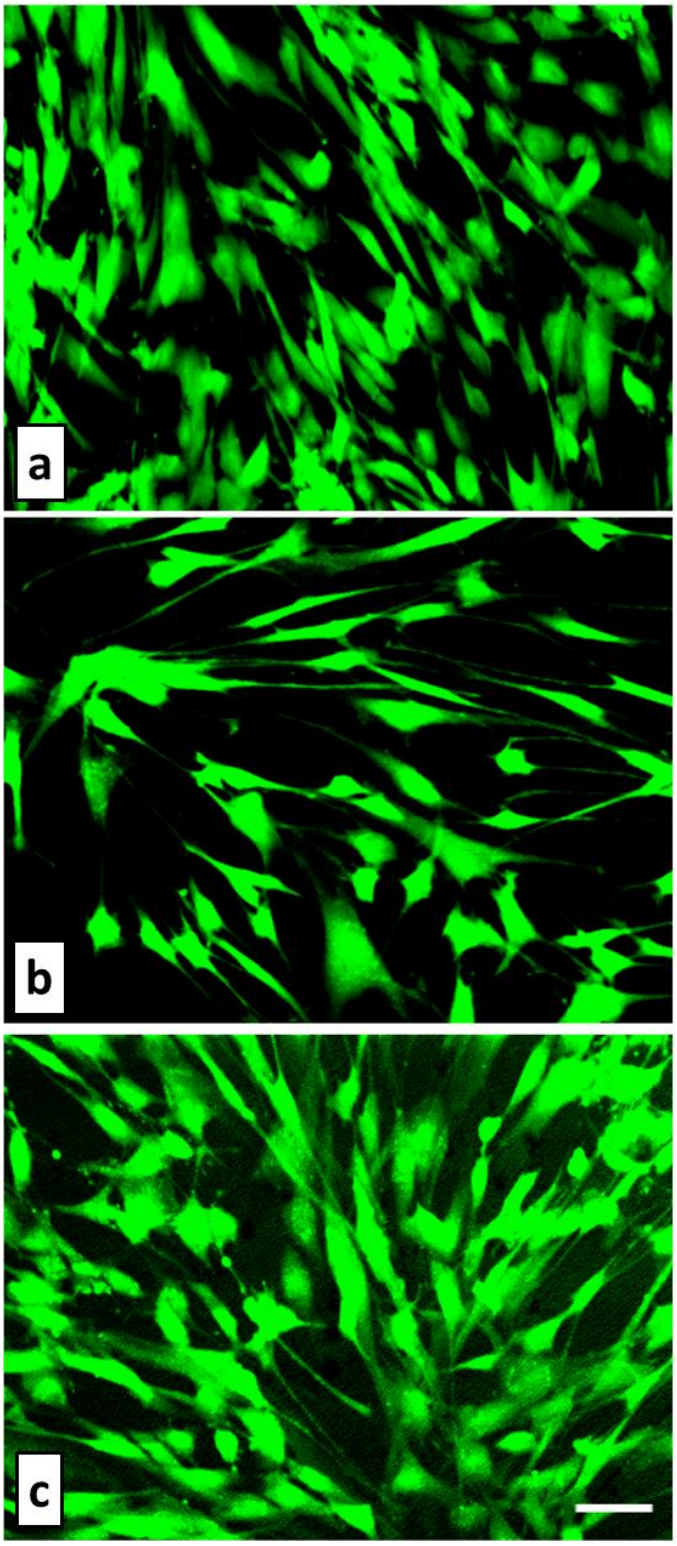

L929 cells were one of the first cells to be established in continuous culture. The line was established already in 1940 and is still the standard for cytotoxicity testing according to ISO 10993 guidelines [44]. MRC-5 cells are of human origin and were established around 30 years later [43].

Several publications suggest that human and rodent primary cells and cell lines derived from both species are equally suitable for the prediction of lethality [74,75]. Our data are in accordance with this assumption because all samples produced similar effects in both murine and human cell lines. It is, therefore, unlikely that these foils cause cell damage *in vivo*.

3.8. Microbiological Properties

All surfaces (uncoated and coated with a-C:H, a-C:H:N, a-C:H:Si, a-C:H:Ti, SiO_x) were investigated according to ISO 22196 [48]. Growth of the test strains was not inhibited. Blue bars in Figure 14 show the number of the inoculated bacteria, red bars show the bacterial cell count after 24 h.

Figure 14. Growth characteristics of (**a**) Staphylococcus aureus DSM 799, (**b**,**d**) Staphylococcus aureus DSM 346 und (**c**,**e**) Escherichia coli DSM 1576 after 24 h on (**a**) on uncoated PEEK with 50 and 100 µm thickness, (**b**,**c**) on 100 µm PEEK foil coated with SiO_x coating, (**d**,**e**) on 100 µm PEEK foil coated with a-C:H, a-C:H:N, a-C:H:Si und a-C:H:Ti coating.

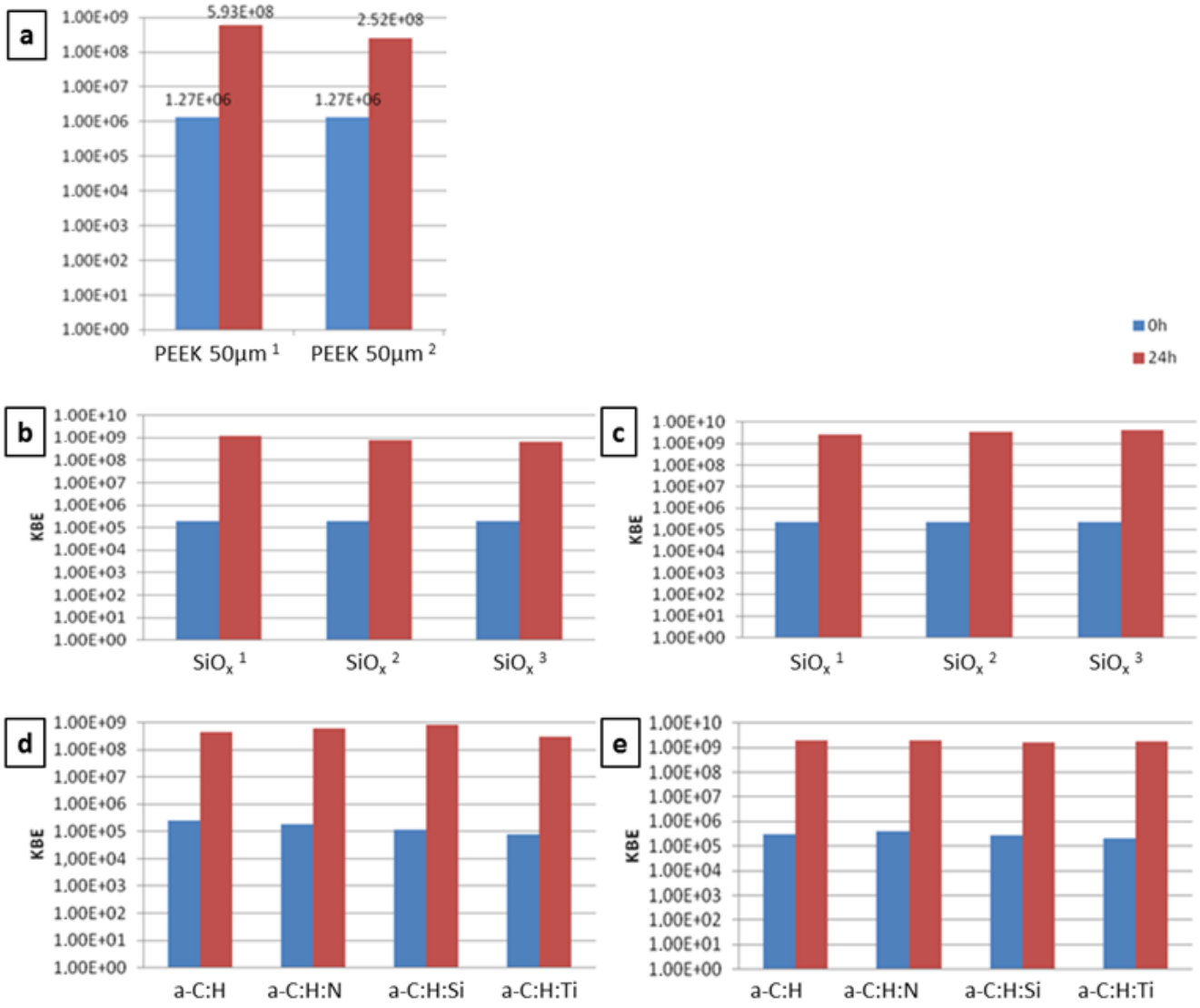

4. Conclusions

Thin films of about 25 nm thickness were deposited on 50 µm thin PEEK foils in order to protect against oxygen permeation through the polymer. Different diamond-like carbon based coating materials, deposited by low-energetic magnetron sputtering and high-energetic direct deposition from ion source plasma were investigated, showing nearly 100 times decreased oxygen transmission rate compared to the uncoated PEEK substrate. The films are not cytotoxic and, as expected, do not influence the microbiology of bacterial growth. Nanowrinkling was found to occur especially in films, deposited from a higher energetic ion source plasma, improving the elastic deformability of these films. While these first results of different diamond-like carbon films prove their applicability as the top layers on future implanted sensors and microelectronic devices in contact to body tissue, some questions are still open (influences of wrinkling nanotopography on protein adsorption due to strong changes in wetting and surface energy).

Acknowledgements

The financial support of this work by the Country of Styria (Austria) in the frame of the program "HTI:SMApp", by the Austrian Research Promotion Agency (FFG) in the frame of the program "Intelligent Production", by the Polish-Austrian exchange project PL 12/2012 (funded in Austria by the Oesterreichischer Austauschdienst, OeAD), and by the European Union is highly acknowledged. The author's thank Harald Parizek and Lukas Volker from JOANNEUM RESEARCH for thin film deposition.

Conflicts of Interest

The authors declare no conflict of interest.

References

1. Mazzuferi, M.; Bovolenta, R.; Bocchi, M.; Braun, T.; Bauer, J.; Jung, E.; Gambari, R. The biocompatibility of materials used in printed circuit board technologies with respect to primary neuronal and K562 cells. *Biomaterials* **2010**, *31*, 1045–1054.
2. Feili, D.; Schuettler, M.; Doerge, T.; Kammer, S.; Stieglitz, T. Encapsulation of organic field effect transistors for flexible biomedical microimplants. *Sensors Actuators A Phys.* **2005**, *120*, 101–109.
3. Makamba, H.; Kim, J.H.; Lim, K.; Park, N.; Hahn, J.H. Surface modification of poly (dimethylsiloxane) microchannels. *Electrophoresis* **2003**, *24*, 3607–3619.
4. Sung, W.C.; Chang, C.C.; Makamba, H.; Chen, S.H. Long-term affinity modification on poly (dimethylsiloxane) substrate and its application for ELISA analysis. *Anal. Chem.* **2008**, *80*, 1529–1535.
5. Walther, M.; Heming, M.; Spallek, M. Multilayer barrier coating system produced by plasma-impulse chemical vapor deposition (PICVD). *Surf. Coatings Technol.* **1996**, *80*, 200–202.
6. Senturia S.D. *Microsystem Design*. Springer Science + Business Media, LLC: New York, NY, USA, 2005.

7. Hedenqvist, M.S.; Johansson, K.S. Barrier properties of SiO_x-coated polymers: Multi-layer modelling and effects of mechanical folding. *Surf. Coatings Technol.* **2003**, *172*, 7–12.
8. Kim, S.R.; Choudhury, M.H.; Kim, W.H.; Kim, G.H. Effects of argon and oxygen flow rate on water vapor barrier properties of silicon oxide coatings deposited on polyethylene terephthalate by plasma enhanced chemical vapor deposition. *Thin Solid Films* **2010**, *518*, 1929–1934.
9. Rochat, G.; Leterrier, Y.; Garamszegi, L.; Månson, J.A.; Fayet, P. Durability of hybrid PECVD-based coatings on semicrystalline polymers. *Surf. Coatings Technol.* **2003**, *174*, 1029–1032.
10. Iwamori, S.; Kita, T.; Saitoh, S.; Yano, S.; Kaminoda, K.; Ohnishi, S.; Suzuki, K. Adhesion and vacuum forming properties of tin–zinc thin films deposited on polyester film substrate. *Vacuum* **2009**, *84*, 581–586.
11. Shim, J.; Yoon, H.G.; Na, S.H.; Kim, I.; Kwak, S. Silicon oxynitride gas barrier coatings on poly (ether sulfone) by plasma-enhanced chemical vapor deposition. *Surf. Coatings Technol.* **2008**, *202*, 2844–2849.
12. Henry, B.M.; Erlat, A.G.; McGuigan, A.; Grovenor, C.R.M.; Briggs, G.A.D.; Tsukahara, Y.; Niijima, T. Characterization of transparent aluminium oxide and indium tin oxide layers on polymer substrates. *Thin Solid Films* **2001**, *382*, 194–201.
13. Charton, C.; Schiller, N.; Fahland, M.; Holländer, A.; Wedel, A.; Noller, K. Development of high barrier films on flexible polymer substrates. *Thin Solid Films* **2006**, *502*, 99–103.
14. Erlat, A.G.; Henry, B.M.; Ingram, J.J.; Mountain, D.B.; McGuigan, A.; Howson, R.P.; Tsukahara, Y. Characterisation of aluminium oxynitride gas barrier films. *Thin Solid Films* **2001**, *388*, 78–86.
15. Chiang, C.C.; Wuu, D.S.; Lin, H.B.; Chen, Y.P.; Chen, T.N.; Lin, Y.C.; Horng, R.H. Deposition and permeation properties of SiN_x/parylene multilayers on polymeric substrates. *Surf. Coatings Technol.* **2006**, *200*, 5843–5848.
16. Kim, N.; Potscavage, W.J.; Domercq, B.; Kippelen, B.; Graham, S. A hybrid encapsulation method for organic electronics. *Appl. Phys. Lett.* **2009**, *94*, 163308:1–163308:3.
17. Hogg, A.; Keppner, H.; Aellen, T.; Burger, J. Ultra-Thin Multi-Layer Protection. US Patent 2011/0039050 A1, 17 February 2011.
18. Hoivik, N.D.; Elam, J.W.; Linderman, R.J.; Bright, V.M.; George, S.M.; Lee, Y.C. Atomic layer deposited protective coatings for micro-electromechanical systems. *Sensors Actuators A Phys.* **2003**, *103*, 100–108.
19. Lackner, J.M.; Waldhauser, W. Diamond and diamond-like carbon coated surfaces as biomaterials. *BHM* **2010**, *155*, 528–533.
20. Butter, R.; Allen, M.; Chandra, L.; Lettington, A.H.; Rushton, N. *In vitro* studies of DLC coatings with silicon intermediate layer. *Diamond Relat. Mater.* **1995**, *4*, 857–861.
21. Linder, S.; Pinkowski, W.; Aepfelbacher, M. Adhesion, cytoskeletal architecture and activation status of primary human macrophages on a diamond-like carbon coated surface. *Biomaterials* **2002**, *23*, 767–773.
22. Mitura, E.; Mitura, S.; Niedzielski, P.; Has, Z.; Wolowiec, R.; Jakubowski, A.; Koczy, B. Diamond-like carbon coatings for biomedical applications. *Diamond Relat. Mater.* **1994**, *3*, 896–898.

23. Allen, M.; Myer, B.; Rushton, N. *In vitro* and *in vivo* investigations into the biocompatibility of diamond-like carbon (DLC) coatings for orthopedic applications. *J. Biomed. Mater. Res.* **2001**, *58*, 319–328.
24. Saito, T.; Hasebe, T.; Yohena, S.; Matsuoka, Y.; Kamijo, A.; Takahashi, K.; Suzuki, T. Antithrombogenicity of fluorinated diamond-like carbon films. *Diamond Relat. Mater.* **2005**, *14*, 1116–1119.
25. Yang, P.; Huang, N.; Leng, Y.X.; Yao, Z.Q.; Zhou, H.F.; Maitz, M.; Chu, P.K. Wettability and biocompatibility of nitrogen-doped hydrogenated amorphous carbon films: Effect of nitrogen. *Nucl. Instrum. Methods Phys. Res. Sec. B Beam Interact. Mater. Atoms* **2006**, *242*, 22–25.
26. Maitz, M.F.; Gago, R.; Abendroth, B.; Camero, M.; Caretti, I.; Kreissig, U. Hemocompatibility of low-friction boron–carbon–nitrogen containing coatings. *J. Biomed. Mater. Res. B Appl. Biomater.* **2006**, *77*, 179–187.
27. Maguire, P.D.; McLaughlin, J.A.; Okpalugo, T.I.T.; Lemoine, P.; Papakonstantinou, P.; McAdams, E.T.; Abbas, G.A. Mechanical stability, corrosion performance and bioresponse of amorphous diamond-like carbon for medical stents and guidewires. *Diamond Relat. Mater.* **2005**, *14*, 1277–1288.
28. Okpalugo, T.I.T.; Ogwu, A.A.; Maguire, P.D.; McLaughlin, J.A.D. Platelet adhesion on silicon modified hydrogenated amorphous carbon films. *Biomaterials* **2004**, *25*, 239–245.
29. Huang, N.; Yang, P.; Leng, Y.X.; Wang, J.; Sun, H.; Chen, J.Y.; Wan, G.J. Surface modification of biomaterials by plasma immersion ion implantation. *Surf. Coatings Technol.* **2004**, *186*, 218–226.
30. *ISO 527-1:2012: Plastics—Determination of tensile properties—Part 1: General principles*; ISO (International Organization for Standardization): Geneva, Switzerland, 2012.
31. Lackner, J.M. Industrially-Scaled Hybrid Pulsed Laser Deposition at Room Temperature. Professorial Dissertation, Institute of Metallurgy and Materials Science, Polish Academy of Science, Kraków, Poland, 2005.
32. Necas, D.; Klapetek, P. Gwyddion: An open-source software for SPM data analysis. *Centr. Eur. J. Phys.* **2012**, 10, 181–188.
33. Teichert, C. Self-organization of nanostructures in semiconductor heteroepitaxy. *Phys. Rep.* **2002**, *365*, 335–432.
34. Sinha, S.K.; Sirota, E.B.; Garoff, S.; Stanley, H.B. X-ray and neutron scattering from rough surfaces. *Phys. Rev. B* **1988**, *38*, 2297–2311.
35. Teichert, C.; Haas, A.; Wallner, G.M.; Lang, R.W. Nanometer Scale Characterization of Polymer Films by Atomic−Force Microscopy. In *Macromolecular Symposia*; Aust, N., Lederer, K., Eds.; WILEY−VCH Verlag GmbH: Weinheim, Germany, 2002; Volume 181, pp. 457–466.
36. Oliver, W.C.; Pharr, G.M. Improved technique for determining hardness and elastic modulus using load and displacement sensing indentation experiments. *J. Mater. Res.* **1992**, *7*, 1564–1583.
37. Li, X.; Diao, D.; Bhushan, B. Fracture mechanisms of thin amorphous carbon films in nanoindentation. *Acta Mater.* **1997**, *45*, 4453–4461.
38. Li, X.; Bhushan, B. Measurement of fracture toughness of ultra-thin amorphous carbon films. *Thin Solid Films* **1998**, *315*, 214–221.

39. Tscherner, M.; Konrad, C.; Bizzarri, A.; Suppan, M.; Cajlakovic, M.; Ribitsch, V.; Stelzer, F. Opto-chemical method for ultra-low oxygen transmission rate measurement. In Proceedings of IEEE SENSORS 2009 Conference, Christchurch, New Zealand, 25–28 October 2009; pp. 1660–1665.
40. Rharbi, Y.; Yekta, A.; Winnik, M.A. A method for measuring oxygen diffusion and oxygen permeation in polymer films based on fluorescence quenching. *Anal. Chem.* **1999**, *71*, 5045–5053.
41. *ISO 10993-1:2009 Biological Evaluation of Medical Devices. Part 1: Evaluation and Testing in the Risk Management Process*; ISO (International Organization for Standardization): Geneva, Switzerland, 2009.
42. *ISO 10993-12:2009 Biological Evaluation of Medical Devices. Part 12: Sample Preparation and Reference Materials*; ISO (International Organization for Standardization): Geneva, Switzerland, 2009.
43. Jacobs, J.P.; Jones, C.M.; Baille, J.P. Characteristics of a human diploid cell designated MRC-5. *Nature* **1970**, *227*, 168–170.
44. Earle, W.R.; Schilling, E.L.; Stark, T.H.; Straus, N.P.; Brown, M.F.; Shelton, E. Production of malignancy *in vitro*. IV. The mouse fibroblast cultures and changes seen in the living cells. *J. Natl. Cancer Inst.* **1943**, *4*, 122–137.
45. *ANIS/AAMI/ISO 10993-5:2009 Biological Evaluation of Medical Devices. Part 5: Tests for in Vitro Cytotoxicity*; ISO (International Organization for Standardization): Geneva, Switzerland, 2009.
46. Van Tienhoven, E.A.E.; Korbee, D.; Schipper, L.; Verharen, H.W.; De Jong, W.H. *In vitro* and *in vivo* (cyto) toxicity assays using PVC and LDPE as model materials. *J. Biomed. Mater. Res. A* **2006**, *78*, 175–182.
47. Biological Reactivity Test, *in Vitro*–Direct Contact Test. In *USP 34-NF 29 The United States Pharmacopeia and National Formulary*; Deutscher Apotheker Verlag: Stuttgart, Germany, 2011.
48. *ISO 22196:2011, Measurement of Antibacterial Activity on Plastics and Other Non-Porous Surfaces*; ISO (International Organization for Standardization): Geneva, Switzerland, 2011.
49. Moulder, J.F.; Stickle, W.F.; Sobol, P.E.; Bomben, K.D. *Handbook of X-ray Electron Spectroscopy*; Marcel Dekker, New York, NY, USA, 1992.
50. Parra, E.R.; Arang, P.J.A.; Palacio, V.J.B. XPS structure analysis of TiN/TiC bilayers produced by pulsed vacuum arc discharge analisis. *Dyna* **2010**, *163*, 64–77.
51. Robertson, J. Structural models of aC and aC:H. *Diamond Relat. Mater*. **1995**, *4*, 297–301.
52. Lackner, J.M.; Waldhauser, W.; Ebner, R.; Lenz, W.; Suess, C.; Jakopic, G.; Hutter, H. Pulsed laser deposition: A new technique for deposition of amorphous SiO_x thin films. *Surf. Coatings Technol.* **2003**, *163*, 300–305.
53. Lackner, J.M.; Waldhauser, W.; Major, L.; Teichert, C.; Hartmann, P. Tribology of bio-inspired nanowrinkled films on ultrasoft substrates. *Comput. Struct. Biotechnol. J.* **2013**, *6*, e201303002.
54. Lackner, J.; Waldhauser, W.; Alamanou, A.; Teichert, C.; Schmied, F.; Major, L.; Major, B. Mechanisms for self-assembling topography formation in low-temperature vacuum deposition of inorganic coatings on polymer surfaces. *Bull. Polish Acad. Sci.* **2010**, 281–294.
55. Lackner, J.M.; Waldhauser, W.; Hartmann, P.; Miskovics, O.; Schmied, F.; Teichert, C.; Schöberl, T. Self-assembling (nano-) wrinkling topography formation in low-temperature vacuum deposition on soft polymer surfaces. *Thin Solid Films* **2012**, *520*, 2833–2840.

56. Lackner, J.M.; Waldhauser, W.; Major, R.; Major, L.; Hartmann, P. Biomimetics in thin film design—Wrinkling and fracture of pulsed laser deposited films in comparison to human skin. *Surf. Coatings Technol.* **2012**, *215*, 192–198.
57. Ohzono, T.; Shimomura, M. Geometry-dependent stripe rearrangement processes induced by strain on preordered microwrinkle patterns. *Langmuir* **2005**, *21*, 7230–7237.
58. Lackner, J.M.; Waldhauser, W.; Schöberl, T. Film growth phenomena in high-energetic room temperature pulsed laser deposition on polymer surfaces. *Surf. Coatings Technol.* **2006**, *201*, 4037–4039.
59. Leyland, A.; Matthews, A. On the significance of the *H*/*E* ratio in wear control: A nanocomposite coating approach to optimised tribological behaviour. *Wear* **2000**, *246*, 1–11.
60. Leyland, A.; Matthews, A. Design criteria for wear-resistant nanostructured and glassy-metal coatings. *Surf. Coatings Technol.* **2004**, *177*, 317–324.
61. Leterrier, Y. Durability of nanosized oxygen-barrier coatings on polymers. *Prog. Mater. Sci.* **2003**, *48*, 1–55.
62. Schrenk, W.J.; Alfrey, T. Some physical properties of multilayered films. *Polymer Eng. Sci.* **1969**, *9*, 393–399.
63. Chatham, H. Oxygen diffusion barrier properties of transparent oxide coatings on polymeric substrates. *Surf. Coatings Technol.* **1996**, *78*, 1–9.
64. Felts, J.T.; Grubb, A.D. Commercial‐scale application of plasma processing for polymeric substrates: From laboratory to production. *J. Vac. Sci. Technol. A* **1992**, *10*, 1675–1681.
65. Burlakov, V.M.; Briggs, G.A.D.; Sutton, A.P.; Tsukahara, Y. Monte carlo simulation of growth of porous SiO_x by vapor deposition. *Phys. Rev. Lett.* **2001**, *86*, 3052–3055.
66. *ISO 10993: Biological Evaluation of Medical Devices*, Part 1–20; ISO (International Organization for Standardization): Geneva, Switzerland, 1997–2012.
67. *EMEA/CHMP/BWP/452081/2007: Guideline on the Replacement of Rabbit Pyrogen Testing by an Alternative Test for Plasma Derived Medicinal Products*; European Medicines Agency: London, UK, 2007.
68. Ronneberger, H.J. Comparison of the pyrogen tests in rabbits and with limulus lysate. *Dev. Biol. Stand.* **1976**, *34*, 27–36.
69. Ekwall, B. Overview of the final MEIC results: II. The *in vitro–in vivo* evaluation, including the selection of a practical battery of cell tests for prediction of acute lethal blood concentrations in humans. *Toxicol.* In Vitro **1999**, *13*, 665–673.
70. *ASTM F813-07 Standard Practice for Direct Contact Cell Culture Evaluation of Materials for Medical Devices*; ASTM International: West Conshohocken, PA, USA, 2012.
71. *ANIS/AAMI/ISO 10993–5:2009: Biological Evaluation of Medical Devices—Part 5: Tests for in Vitro Cytotoxicity*; AAMI (Association for the Advancement of Medical Instrumentation): Arlington, VA, USA, 2009.
72. Scudiero, D.A.; Shoemaker, R.H.; Paull, K.D.; Monks, A.; Tierney, S.; Nofziger, T.H.; Boyd, M.R. Evaluation of a soluble tetrazolium/formazan assay for cell growth and drug sensitivity in culture using human and other tumor cell lines. *Cancer Res.* **1988**, *48*, 4827–4833.
73. Department of Health, Education, and Welfare Public Health Service; Food and Drug Administration. *Bacterial Endotoxins/Pyrogens*, Inspection Guides. Available online:

http://www.fda.gov/ICECI/Inspections/InspectionGuides/InspectionTechnicalGuides/ucm072918.htm (access on 28 August 2013).

74. Halle, W.; Spielmann, H. Two procedures for the prediction of acute toxicity (LD50) from cytotoxicity data. ATLA. *Altern. Lab. Animals* **1992**, *20*, 40–49.
75. *Report of the International Workshop on* in Vitro *Methods for Assessing Acute Systemic Toxicity*, NIH Publication 01-4499; NIEHS (National Institute of Environmental Health Sciences), Research Triangle Park, NC, USA, 2001.